



# Maximization of photocatalytic activity of $\text{Bi}_2\text{S}_3/\text{TiO}_2/\text{Au}$ ternary heterostructures by proper epitaxy formation and plasmonic sensitization



Sumana Paul<sup>1</sup>, Sirshendu Ghosh<sup>1,2</sup>, Dulal Barman, S.K. De\*

Department of Materials Science, Indian Association for the Cultivation of Science, Kolkata, 700032, India

## ARTICLE INFO

### Article history:

Received 12 March 2017

Received in revised form 4 July 2017

Accepted 19 July 2017

Available online 22 July 2017

### Keywords:

Hybrid nanoheterostructure

$\text{Bi}_2\text{S}_3/\text{TiO}_2/\text{Au}$

Epitaxy formation

Photocatalyst

Plasmonic sensitization

## ABSTRACT

Ternary  $\text{Bi}_2\text{S}_3/\text{TiO}_2/\text{Au}$  heterostructure has been successfully synthesized by decorationg Au nanoparticles onto binary  $\text{Bi}_2\text{S}_3/\text{TiO}_2$  heterostructure. Structural analysis suggests that the heterostructure consists of orthorhombic  $\text{Bi}_2\text{S}_3$ , tetragonal anatase  $\text{TiO}_2$  and face centered cubic Au. The appearance of extra Raman peak at  $123\text{ cm}^{-1}$  and the modification of Raman peaks of  $\text{Bi}_2\text{S}_3$  and  $\text{TiO}_2$  phases indicates a significant molecular interaction during growth of  $\text{TiO}_2$  nanocrystals (NCs) on the surface of  $\text{Bi}_2\text{S}_3$  nanorods. Self assembly of nanorods triggered by oleic acid results in urchin like morphology of pure  $\text{Bi}_2\text{S}_3$ . The {011} facet of  $\text{TiO}_2$  nanocrystals grow epiaxially on {013} facet of  $\text{Bi}_2\text{S}_3$  nanorods. Periodic arrangement of (111) plane of Au and (011) plane of  $\text{Bi}_2\text{S}_3$  favors epitaxial growth in  $\text{Bi}_2\text{S}_3/\text{TiO}_2/\text{Au}$  heterostructure. Unique design of the ternary heterostructure makes a preferable pathway for the photogenerated electrons by suppressing the electron-hole recombination. The observation of decreased electron spin resonance signal intensity based on spin label technique confirms the electron transfer from photoexcited heterostructure. Favorable energetic positions of conduction and valence band edges of semiconductors ( $\text{Bi}_2\text{S}_3$  and  $\text{TiO}_2$ ) and Fermi level of metal (Au) are the key factors to enhance the photo catalytic activity of ternary heterostructure. Plasmonic phenomenon of metal (Au) nanoparticles by changing their size and shape was also investigated to remove organic pollutants from waste water.

© 2017 Elsevier B.V. All rights reserved.

## 1. Introduction

For cleaner and greener world, development of green photocatalyst is very important for alternative energy source like  $\text{H}_2$  gas production by water splitting and degradation of hazardous organic dyes which are used daily for betterment of human life. In present situation of nanoscience research, nanoscale metal-semiconductor and semiconductor-semiconductor hybrid heterostructures with various morphology and tuneable size are most emerging candidates for solar energy conversion, photocatalysis and optoelectronic devices [1–4]. To be a potent candidate to show excellent photoactivity, efficient charge separation in semiconductor is very essential. Under the band gap excitation, electron-hole (e-h) pair (exciton pairs) is formed both in bulk and surface. But exciton pair formed in bulk is not useful, as the photo-

catalysis process is a surface phenomenon in semiconductors. Migration of exciton from bulk to surface site is often slow and they normally recombine in midway. So increase the surface area by lowering the dimension of semiconductor is one of the fruitful way to improve the efficiency of photocatalytic activity [5]. Among the green oxides,  $\text{TiO}_2$  and  $\text{ZnO}$  are the most promising candidates for their high earth abundance [6,7].  $\text{TiO}_2/\text{ZnO}$  allows the formation of an e-h pair only when irradiated by ultra-violet (UV) light of the whole solar light spectrum. But in terms of available energy, visible (43%) and infrared (52%) light constitute most of the solar emission with a very low amount of UV (4%) light [8]. This is the biggest problem for maximum solar photon utility of most commercialised  $\text{TiO}_2$  based photocatalyst P25. Also the high recombination rate of photo-generated electron and hole in  $\text{TiO}_2$  often leads to a low quantum yield and poor photo catalytic activity. Different efforts have been taken to overcome the limitation of titania, such as doping, decreasing the crystallite size and photosensitization of  $\text{TiO}_2$ . The band gap can be decreased by doping but the process has some disadvantages: (i) introduction of impurity can strongly affect the life time of e-h pair and might act as recombination centre, (ii) doping also can decrease the corrosion resistance of the  $\text{TiO}_2$  (especially when

\* Corresponding author.

E-mail addresses: [msskd@iacs.res.in](mailto:msskd@iacs.res.in), [skdiacs@gmail.com](mailto:skdiacs@gmail.com) (S.K. De).

<sup>1</sup> Authors contributed equally.

<sup>2</sup> Present address: Department of Chemistry, National Cheng Kung University, Tainan, Taiwan.

the dopant is transition metal ions). Although the attachment of organic dyes with  $\text{TiO}_2$  is somehow fruitful [9,10] for photosensitization of  $\text{TiO}_2$  but still face major problems in photocatalysis like poor stability of dye which can undergo oxidative degradation of dyes or fast back electron transfer.

Recent researches [11,12] established that combination of wide band gap photocatalyst with narrow band gap semiconductors like metal chalcogenides might be an effective way to harvest solar light on a broad scale which also prompts the charge separation and results in high photocatalytic activity like  $\text{H}_2$  generation [13]. Metal sulfide- $\text{TiO}_2$  nanoheterostructures (NHS) including  $\text{PbS-TiO}_2$ ,  $\text{WS}_2\text{-TiO}_2$ ,  $\text{MoS}_2\text{-TiO}_2$ ,  $\text{FeS}_2\text{-TiO}_2$  and  $\text{CdS-TiO}_2$  exhibit high photocatalytic activity and photovoltaic performances [14–17,12]. Fang et al. has reported [18] high yield  $\text{H}_2$  generation in  $\text{Au@TiO}_2\text{-CdS}$  ternary NHS. Although  $\text{CdS}$  is a promising candidate for enhancing the photoactivity of  $\text{TiO}_2$  but it faces toxicity problem of  $\text{Cd}$ . Bismuth sulfide ( $\text{Bi}_2\text{S}_3$ ) can be a better substitution as it has an absorbance onset at  $\sim 1.3\text{--}1.5\text{ eV}$  with high absorbance coefficient ( $10^4\text{ cm}^{-1}$ ) [19]. Thus  $\text{Bi}_2\text{S}_3$  is able to harvest visible light from the solar spectrum and a greener material too.  $\text{Bi}_2\text{S}_3$  is an excellent photoconductive semiconductor and a promising candidate for electrochemical hydrogen storage, hydrogen sensing and biomolecule detection. But severe recombination of photogenerated e-h is a major problem which results in low quantum yield. Complete e-h separation can be done by attachment of metal or semiconductor NCs onto  $\text{Bi}_2\text{S}_3$  surface having proper band alignment. As the conduction band (CB) energy level of  $\text{Bi}_2\text{S}_3$  is 0.26 eV higher than  $\text{TiO}_2$ , the photo generated electrons can be smoothly transferred from  $\text{Bi}_2\text{S}_3$  to  $\text{TiO}_2$ . Whereas valence band (VB) of  $\text{TiO}_2$  is lower than that of  $\text{Bi}_2\text{S}_3$ , so photogenerated hole can be transferred to  $\text{Bi}_2\text{S}_3$ . So complete separation of e-h in both  $\text{TiO}_2$  and  $\text{Bi}_2\text{S}_3$  is possible and  $\text{Bi}_2\text{S}_3\text{/TiO}_2$  NHS results in a type-II band alignment [20,21]. Previous reported  $\text{Bi}_2\text{S}_3\text{/TiO}_2$  reveals visible light induced hydrogen evolution and photocatalytic activity but not such a higher extent than pure  $\text{Bi}_2\text{S}_3$  or  $\text{TiO}_2$  [22]. Most of these reports demonstrated the uncontrolled deposition of  $\text{Bi}_2\text{S}_3$  onto  $\text{TiO}_2$  surface without any proper epitaxy. Efficient e-h separation is only possible if  $\text{TiO}_2$  and  $\text{Bi}_2\text{S}_3$  are connected by an epitaxial crystallographic relation. The absorbance features of  $\text{Bi}_2\text{S}_3$  highly depend upon its dimension. Zero dimensional  $\text{Bi}_2\text{S}_3$  nanodots are capable of only absorbing the UV light for the strong 3D quantum confinement effect. Whereas 1-D nanowire/rod and 2-D nanosheet morphology can absorb in broad spectrum area from visible (VIS) to near infrared (NIR) region [23,24]. So, for the maximisation of photocatalytic property of  $\text{Bi}_2\text{S}_3\text{/TiO}_2$  NHS, exact morphology with epitaxial growth of one onto another is highly necessary. One dimensional structure can offer a direct path for the photogenerated charges, resulting in superior charge transport properties for large surface area. Previous result also suggests [25] that hierarchical morphology is facile for dye adsorption as they have high surface area.

Here we have synthesized  $\text{Bi}_2\text{S}_3$  nanourchin by the self assembly of  $\text{Bi}_2\text{S}_3$  nanorods. Controlled synthesis and suitable use of additives resulted in a highly monodispersed  $\text{Bi}_2\text{S}_3$  nanourchin.  $\text{Bi}_2\text{S}_3\text{/TiO}_2$  NHS has been synthesized by two step process. Hydrothermal treatment of  $\text{Bi}_2\text{S}_3$  nanourchin with Ti-precursor resulted in  $\text{Bi}_2\text{S}_3\text{/TiO}_2$  NHS, where anatase  $\text{TiO}_2$  NCs is uniformly anchored.

From our previous research and literature survey [25–28], we have found another way to maximise the photoactivity of semiconductor is the attachment of metal nanocrystals. Metal NCs can act as an electron sink and can accept photogenerated electrons from semiconductor resulting in the increment of exciton life time. Our recent research predicts [25,26] that formation of metal-semiconductor epitaxy formation is crucial for efficient charge separation. Metal NCs can often extend the light absorption of semiconductor. Localised surface plasmon resonance (LSPR) corresponds to the collective oscillation of surface electrons with an

oscillation frequency that depends upon metal nanocrystal size, shape and degree of alloying. Metal nanocrystals can act as a nanoantenna which can enhance electric field at the surrounding (0–40 nm) medium. As the optical absorbance of semiconductor depends on intensity of the perturbation electric field, so presence of metal NC in close vicinity can enhance absorbance intensity. The enhanced energy due to plasmon in metal can be transferred directly by transfer of electrons to semiconductors ('hot' electron). Another mechanism is plasmon induced resonance energy transfer (PIRET). In PIRET, the plasmonic resonance excites electron–hole pairs in the semiconductor by coupling between the plasmonic dipole in the metal and electron–hole pair dipole of semiconductor.

Enhancement of photoactivity is already observed in ternary heterostructures composed of QDs, metal NCs and oxide semiconductor nanoparticles [29]. The plasmonic photosensitization effect in our developed  $\text{Bi}_2\text{S}_3\text{/TiO}_2$  is not reported yet. We have also studied the photo conversion enhancement by altering the Au nanoparticles size/shape in these newly formed ternary structures to get beyond the best result.

## 2. Experimental section

### 2.1. Materials

Bismuth nitrate ( $\text{Bi}(\text{NO}_3)_3\text{,5H}_2\text{O}$ ), sodium diethyldithiocarbamate ( $\text{Na}[\text{S}_2\text{CNEt}_2]$ ), ethanol, oleic acid (OA), chloroauric acid, tetrachloroethelene (TCE), toluene, rhodamine B (RhB) dye, potassium dichromate ( $\text{K}_2\text{Cr}_2\text{O}_7$ ), diphenylcarbazide, citric acid, acetone all reagents were of analytical grade and purchased from MERCK. Oleylamine (OLAM), titanium butoxide, dodecanthiol, tri ethylorthosilicate (TEOS), butylamine were purchased from Sigma Aldrich. All reagents were used as purchased without further purification. DI water was used throughout all the experiments.

### 2.2. Preparation of bismuth diethyldithiocarbamate complex ( $\text{Bi}(\text{S}_2\text{CNEt}_2)_3$ )

In a typical synthesis procedure 3.39 mmol of Bismuth nitrate ( $\text{Bi}(\text{NO}_3)_3\text{,5H}_2\text{O}$ ) was dissolved in 25 ml of ethanol to form a homogeneous solution. Then, 40 ml ethanol solution containing 10 mmol sodium diethyldithiocarbamate ( $\text{NaS}_2\text{CNEt}_2$ ) was added dropwise to the previous solution under vigorous stirring. A bright yellow colloid suspension was formed instantly. After 2 h of vigorous magnetic stirring the yellow colored precipitate was collected by centrifugation. The powder was dried for 4 h at 60 °C before further use.

### 2.3. Preparation of bismuth sulfide ( $\text{Bi}_2\text{S}_3$ ) nanorods assembly

Bismuth sulfide nanorod assembly was synthesized by decomposition of bismuth diethyldithiocarbamate complex in a mixed solvent of oleylamine (OLAM) and oleic acid (OA). In a typical synthesis procedure 0.17 mmol of bismuth diethyldithiocarbamate, 1.5 ml of OLAM, 4 ml of OA, 0.523 ml of dodecanthiol were mixed in 25 ml round bottom three neck flask fitted with a reflux condenser. The system was evacuated for 15 min at room temperature. After that the temperature was increased to 90 °C slowly under constant evacuation condition. Then  $\text{N}_2$  gas was purged into the solution and the temperature was increased to 160 °C and the reaction was continued for another 15 min. The black colored solution was then cooled down to room temperature and washed with toluene and excess ethanol. The product was centrifuged at 10,000 rpm for 3 min and the centrifugation was repeated for 3–4 times to remove impurities. The product was redispersed in nonpolar solvent like TCE, toluene etc.

#### 2.4. Preparation of $\text{Bi}_2\text{S}_3/\text{TiO}_2$ heterostructures

$\text{Bi}_2\text{S}_3/\text{TiO}_2$  heterostructures were synthesized through a simple hydrothermal procedure. In a typical reaction, 35 mg of  $\text{Bi}_2\text{S}_3$  was dispersed in a mixed solvent containing 3 ml of toluene, 2.6 ml of OA, 1.8 ml of OLAM, 8 ml of ethanol. Then 0.463 ml of titanium butoxide was added to the mixed solution. The mixed solution was treated by sonication for 5 min and then transferred into a Teflon-lined stainless steel autoclave, heated at 180 °C for 24 h. The autoclave was air-cooled to room temperature. The obtained black powders were centrifuged and washed thoroughly with ethanol and dried at 50 °C for 12 h. The composition of  $\text{Bi}_2\text{S}_3/\text{TiO}_2$  was varied by changing the mole percentage ratio of Bi:Ti. Three nanoheterostructures NHS1, NHS2, NHS3 were synthesized where Bi:Ti ratio were 1:0.5, 1:1.33 and 1:4 respectively.

#### 2.5. Preparation of $\text{Au}@\text{Bi}_2\text{S}_3/\text{TiO}_2$ heterostructure

Gold nanoparticle decorated  $\text{Bi}_2\text{S}_3/\text{TiO}_2$  composite was prepared using a facial method. In this procedure 35 mg of composite was dispersed in 5 ml of toluene in a 25 ml round bottom flask with a condenser. 0.033 gm of chlroauric acid dissolved in 1 ml of toluene and 0.6 ml of OLAM was used as gold stock solution and it was added to the above mixed solution. The solution was stirred for 10 min at room temperature. Then the temperature was increased to 70 °C and kept at this temperature for 15 min. The solution was then cooled to room temperature and collected by centrifugation by adding excess ethanol.

### 3. Characterization

The crystalline phases of the products were determined by X-ray powder diffraction (XRD) by using a Bruker AXS D8SWAX diffractometer, with Cu K $\alpha$  radiation ( $\lambda = 1.54\text{ \AA}$ ), employing a scanning rate of  $0.5^\circ \text{ S}^{-1}$  in the  $2\theta$  range from  $20^\circ$  to  $60^\circ$ . For XRD measurement the TCE solution of the NCs was drop cast over an amorphous silicon sample holder till a thin layer visible to the naked eye was formed. Transmission electron microscopy (TEM) images, high angle annular dark field scanning TEM (HAADF-STEM) images and energy dispersive spectra (EDS), elemental mapping were taken using an ultra-high resolution field emission gun transmission electron microscope (UHR-FEG TEM, JEM-2100F, Jeol, Japan) operating at 200 kV. For the TEM observations, the sample was dissolved in TCE and was drop cast on a carbon coated copper grid. The room temperature optical absorbance of the samples was measured by a Varian Cary 5000 UV-VIS-NIR spectrometer. Room temperature photoluminescence (PL) measurements were carried out with a fluorescence spectrometer (Hitachi, F-2500). Valence state analysis was carried out by an X-ray photoelectron spectroscopic (XPS, Omicron, model: 1712-62-11) method. XPS measurements were done using an Al-K $\alpha$  radiation source under 15 kV voltage and 5 mA current. For XPS measurements the hexane solution of NCs was drop cast over a Si chip ( $2\text{ mm} \times 2\text{ mm}$ ) till a naked eye visible thin layer was formed.

### 4. Photocatalytic test

#### 4.1. Photocatalytic degradation test of rhodamine B

For the photocatalytic degradation of RhB, 10 mg of sample was dispersed in 3 ml of toluene. In another vial 10 ml of 0.0008 mM aqueous solution of RhB was prepared. After that solution containing catalyst was poured into the aqueous solution of dye. Then the bi-phasic mixture was stirred for 5 min in dark for equilibrium mixing. Then the solution was irradiated with a light source (KRATOS,

Analytical instruments, universal arc lamp supply: 250 W, 150XE, model no. 1152). The aqueous part of the bi-phasic mixture was collected at a regular interval of time and centrifuged. The absorbance measurement of the solution was conducted using a Varian Cary 5000 UV-VIS-NIR spectrophotometer. The photocatalytic experiment of RhB was also conducted in presence of selective excitation wavelength using light emitting diode (LED) to identify contribution of individual semiconductor.

#### 4.2. Reduction of 4-nitrophenol

For the reduction of 4-nitrophenol (4-NP), 15 ml 0.01 mM aqueous solution of 4-NP was prepared. A freshly prepared aqueous solution of  $\text{NaBH}_4$  (0.162 gm) was added to the aqueous solution of 4-NP. After that 6 mg of catalyst was added to start reaction. The absorbance measurements were carried by the same procedure as described in case of RhB.

#### 4.3. Detection of Cr(VI)

In a typical experiment, 5 ml of a 10 ppm solution of chromium (Cr(VI)) was prepared by dissolving  $\text{K}_2\text{Cr}_2\text{O}_7$  salt in DI water. Next, 0.39 mM citric acid was added to the Cr(VI) solution, followed by maintaining a constant pH of 2 using a 1 M HCl solution. A violet color was developed in the Cr(VI) solution via the addition of a 19.77 mM diphenylcarbazide solution in acetone. After color change, 2 mg of catalyst was added to the solution, and the resulting mixture was ultrasonicated for 4 min followed by incubation in the dark for 30 min under stirring to achieve adsorption-desorption equilibrium. Then the reaction mixture was irradiated with the light source previously mentioned. The reaction mixture was discarded at various interval of time and centrifuged. The concentration of Cr(VI) was measured with a spectrophotometer at  $\lambda = 540\text{ nm}$  (Varian Cary 5000 UV-VIS-NIR spectrophotometer) using the diphenylcarbazide method.

### 5. Electron spin resonance (ESR) spectroscopy

The ESR measurements of spin label 2,2,6,6-tetramethyl-1-piperidinyloxy (TEMPO) were carried out at 77 K by JEOL (JES FA200) spectrophotometer using X-band (9.8 GHz) microwave source. 500  $\mu\text{l}$  of control or sample solutions in toluene were put in quartz capillary tubes which were then sealed. The capillary tubes were put into the ESR cavity, and the spectra were obtained after 10 min of irradiation.

### 6. Device fabrication

Thin films for photocatalytic test were prepared by a multi step process. First of all glass substrates ( $1\text{ cm} \times 1\text{ cm}$ ) were cleaned by standard protocol and after that they were ultra sonicated for 15 min in a mixture of acetone and isopropyl alcohol. After that the substrates were dried in 60 °C in a hot air oven.

Au nanoparticles (Au NP) and Au nanorods (Au NR) were synthesized by previously mentioned method [30,31]. Long chain of ligands of gold nanoparticles (Au NP),  $\text{Bi}_2\text{S}_3/\text{TiO}_2$  composites was replaced by ligand exchange process. For this 0.5 ml of butylamine dissolved in 3 ml of acetonitrile and the 3 ml of sample solution in hexane was added to it. After that the mixture was sonicated for 5 min and centrifuged. Then they were dispersed in hexane. Long chain of cetyl trimethylammonium bromide (CTAB) capped gold nanorods (Au NRs) were removed by 20 min centrifugation and finally dispersed in hexane.

1 mg of Au NP/Au NR dispersed in hexane was spin casted onto the glass substrates to form a 2D array of gold nanoparticles. After

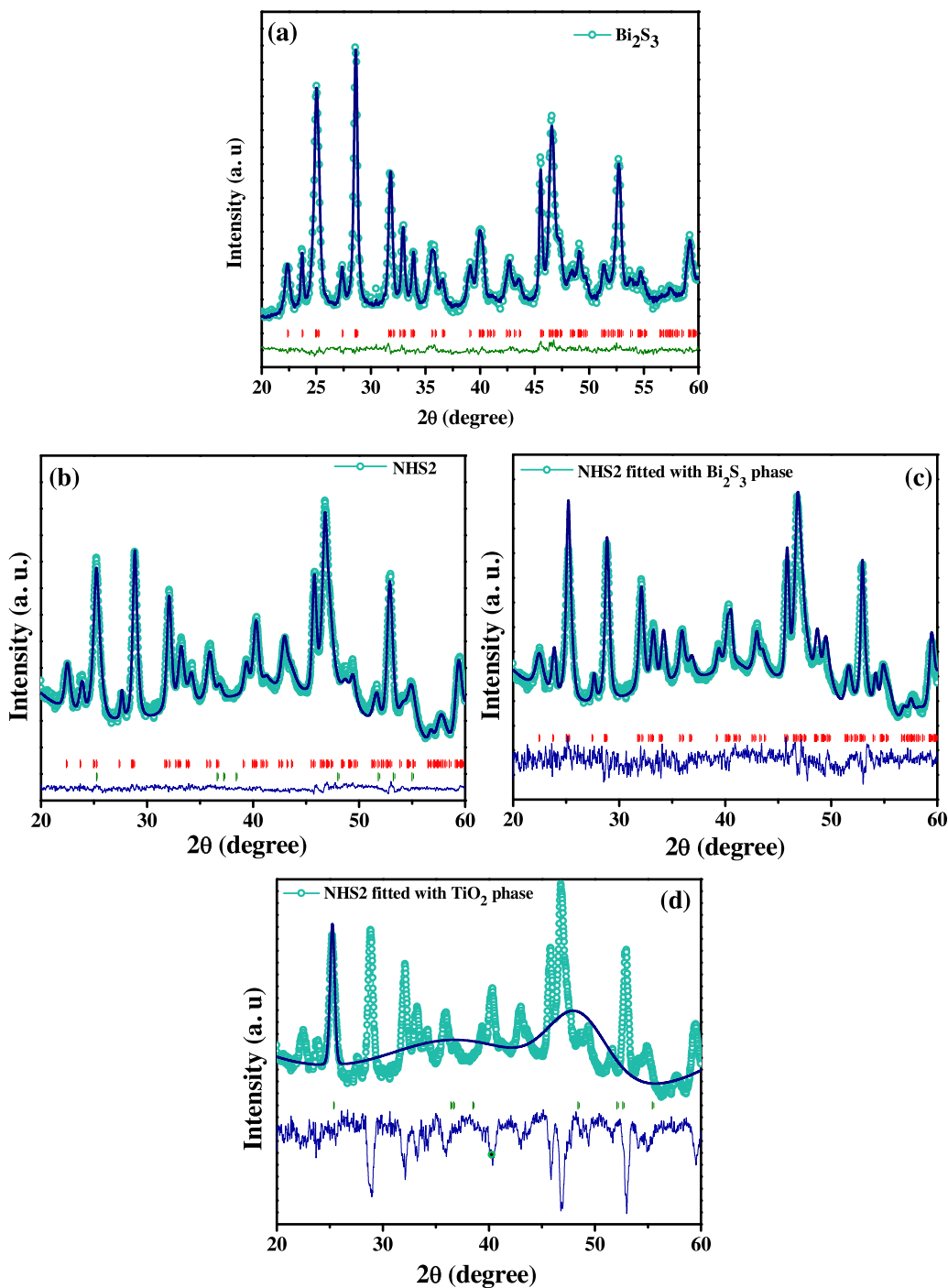


**Fig 1.** Typical Rietveld Refinement output pattern of  $\text{Bi}_2\text{S}_3/\text{TiO}_2$  nanoheterostructures. (a) Orthorhombic pure  $\text{Bi}_2\text{S}_3$  phase only. (b) fitted by NHS2 only. (c) XRD of NHS2 fitted with  $\text{Bi}_2\text{S}_3$  phase only. (d) XRD of NHS2 fitted with  $\text{TiO}_2$  only.

that the gold layer was functionalized by depositing a thin layer of tri ethylorthosilicate (TEOS). 20  $\mu\text{l}$  of TEOS solution in methanol in 1% (v/v) was spin casted onto the thin layer of gold. TEOS here acted as an anchoring agent as well as a dielectric layer. After that 1 mg sample ( $\text{Bi}_2\text{S}_3/\text{TiO}_2$  composites) dispersed in toluene were spin casted above each of the thin film device.

Now, in order to test photocatalytic activity of our device, it was illuminated with different light such as UV light, red LED, green LED lights. Samples for photocatalytic degradation of RhB 40  $\mu\text{l}$  of methanolic solution of Rh B (0.0008 mM) was drop casted upon the device and dried the device at 90 °C at hot air oven. All the experiments were done in presence of air as oxygen acts as an electron

scavenger. Now to evaluate photocatalytic activity, the samples discarded for regular interval of time and their excitonic spectra were recorded by a Varian Cary 5000 UV-VIS-NIR spectrophotometer.

## 7. Results and discussion

### 7.1. XRD analysis

Phases of the as prepared  $\text{Bi}_2\text{S}_3$  nanorod (NR) assembly,  $\text{TiO}_2$  NPs,  $\text{Bi}_2\text{S}_3/\text{TiO}_2$ ,  $\text{Au}@\text{Bi}_2\text{S}_3$  and  $\text{Au}@\text{Bi}_2\text{S}_3/\text{TiO}_2$  heterostructures were identified by XRD analysis. Fig. 1a shows the XRD pattern of  $\text{Bi}_2\text{S}_3$  NR assembly, with all peaks correspond to orthorhombic

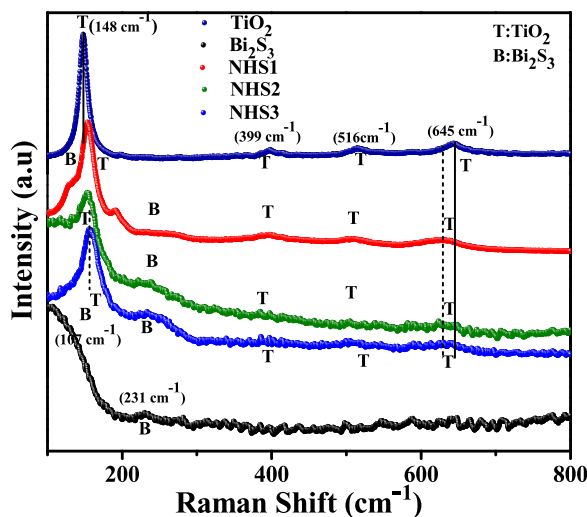


Fig. 2. Raman spectra of different nanoheterostructures.

$\text{Bi}_2\text{S}_3$  (JCPDS file No: 43-1471, space group  $Pnma$ , lattice parameters  $a = 11.305 \text{ \AA}$ ,  $b = 3.981 \text{ \AA}$ ,  $c = 11.147 \text{ \AA}$ ). Rietveld refinement of XRD pattern for  $\text{Bi}_2\text{S}_3$  NR assembly suggests that the lattice parameters, are:  $a = 11.306 \text{ \AA}$ ,  $b = 3.985 \text{ \AA}$  and  $c = 11.158 \text{ \AA}$  slightly larger than the bulk value (Table S1). The unit cell volume of NRs increases from  $501.67 \text{ \AA}^3$  to  $502.71 \text{ \AA}^3$  as the particle size reduces to nano-size regime. The diffraction peaks of pure  $\text{TiO}_2$  NPs shown in the supporting information (SI) Fig. S1a, identified as the tetragonal anatase  $\text{TiO}_2$  (JCPDS file No: 84-1285, space group  $I41/amd$ , lattice parameters  $a = 3.776 \text{ \AA}$ ,  $c = 9.486 \text{ \AA}$ ). The XRD pattern of  $\text{Bi}_2\text{S}_3/\text{TiO}_2$  heterostructures (SI Fig. S1b and S1c) is almost similar to that of  $\text{Bi}_2\text{S}_3$  except the relative intensity of the peaks at  $2\theta = 25.1^\circ$  (310) plane and  $28.5^\circ$  (121) plane of pure  $\text{Bi}_2\text{S}_3$ . This variation in the intensity of (310) and (121) plane is due to the overlapping of (310) plane of  $\text{Bi}_2\text{S}_3$  and (101) plane (at  $2\theta = 25.3^\circ$ ) of  $\text{TiO}_2$ .

The XRD pattern of  $\text{Au}@\text{Bi}_2\text{S}_3$  and  $\text{Au}@\text{Bi}_2\text{S}_3/\text{TiO}_2$  (SI, Fig. S1d) reveals a peak at  $2\theta = 38.2^\circ$  which corresponds to (111) plane of face centered cubic (fcc)  $\text{Au}$  (JCPDS file No:01-1174). In brief,

the ternary composite material consists of fcc  $\text{Au}$ , anatase  $\text{TiO}_2$  and orthorhombic  $\text{Bi}_2\text{S}_3$ . Moreover XPS spectra were obtained to further investigate the presence of  $\text{Au}$  in the nanoheterostructure  $\text{Au}@\text{NHS2}$  (NHS2 implies  $\text{Bi}_2\text{S}_3/\text{TiO}_2$  heterostructure where  $\text{Bi}:\text{Ti} = 1:1.33$ ). Fig. S2a in SI shows the XPS spectra of  $\text{Au} 4f$ . Two well resolved peaks at  $84.0 \text{ eV}$  and  $87.7 \text{ eV}$  are consistent with the binding energies of  $\text{Au} 4f_{7/2}$  and  $\text{Au} 4f_{5/2}$  respectively with a separation of  $3.7 \text{ eV}$ . These values confirm that gold is present in the nanoheterostructure in the metallic  $\text{Au}(0)$  state [32]. To investigate the structural overlapping of two phases in a multiphasic material, Rietveld analysis is an useful method. We can see a high intensity mismatch when XRD pattern of NHS2 (Fig. 1b) was fitted with orthorhombic  $\text{Bi}_2\text{S}_3$  and tetragonal  $\text{TiO}_2$  separately (Fig. 1c and d). But the poor Rietveld refinement data significantly improves when we consider 80 vol% of  $\text{Bi}_2\text{S}_3$  and 20 vol% of  $\text{TiO}_2$ . This good fitted data suggest that there must be an overlapping of (310) plane of  $\text{Bi}_2\text{S}_3$  and (101) plane of  $\text{TiO}_2$ .

## 8. Raman spectroscopy

To further identify the individual phases and crystallinity of the as prepared samples Raman Spectra were collected in the wavenumber range  $100$ – $800 \text{ cm}^{-1}$  as shown in Fig. 2. The Raman peaks are indicated by letter 'T' for  $\text{TiO}_2$  and letter 'B' for  $\text{Bi}_2\text{S}_3$ . There are four Raman active modes of orthorhombic  $\text{Bi}_2\text{S}_3$ :  $A_g$ ,  $B_{1g}$ ,  $B_{2g}$  and  $B_{3g}$  and one IR active mode  $B_{3u}$  which have been theoretically calculated by Tanner et al. [33]. The Raman spectrum of pure  $\text{Bi}_2\text{S}_3$  reveals a broad hump in between  $100$  and  $200 \text{ cm}^{-1}$  and a short hump at  $231 \text{ cm}^{-1}$  which corresponds to theoretically predicted Ag optical phonon mode of  $\text{Bi}_2\text{S}_3$ , associated with the transverse phonon modes.  $\text{Bi}_2\text{S}_3$  is well known for its low thermal conductivity [34] and therefore we obtained the Raman spectra at lower laser power. Raman features of  $\text{Bi}_2\text{S}_3$  are very sensitive to thermal power and at low excitation power these modes are indistinguishable or appeared as broad hump [33]. We noticed that in case of pure  $\text{TiO}_2$ , there are four characteristic Raman peaks appeared at  $148 \text{ cm}^{-1}$ ,  $399 \text{ cm}^{-1}$ ,  $516 \text{ cm}^{-1}$  and  $645 \text{ cm}^{-1}$ . It confirms that typical anatase  $\text{TiO}_2$  phase has been formed. The peaks at  $148 \text{ cm}^{-1}$  and  $645 \text{ cm}^{-1}$  are the characteristic  $E_g$  peaks which arise due to the symmetric stretching vibration of O-Ti-O in  $\text{TiO}_2$ . The peak

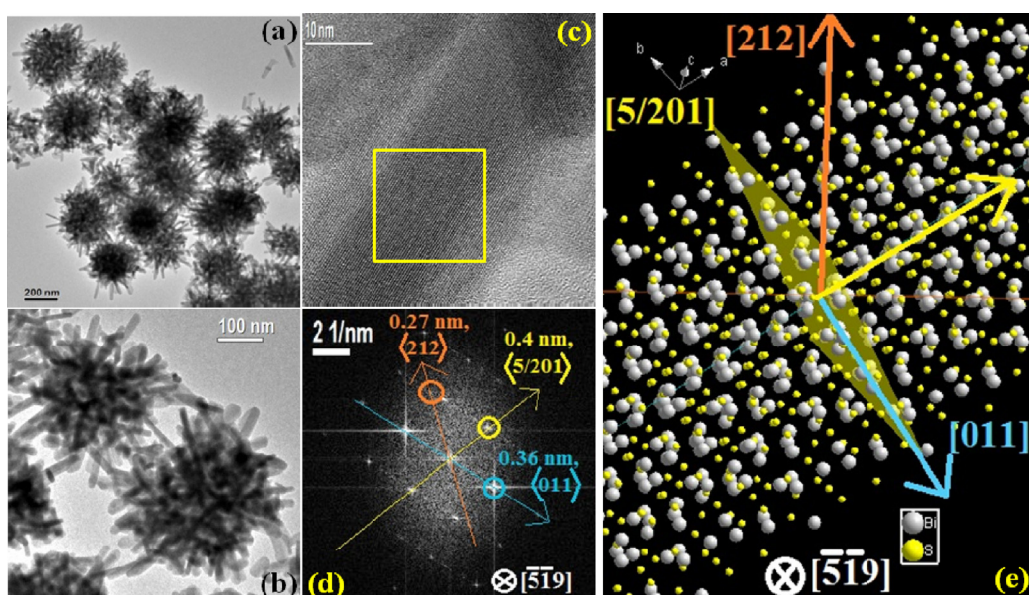
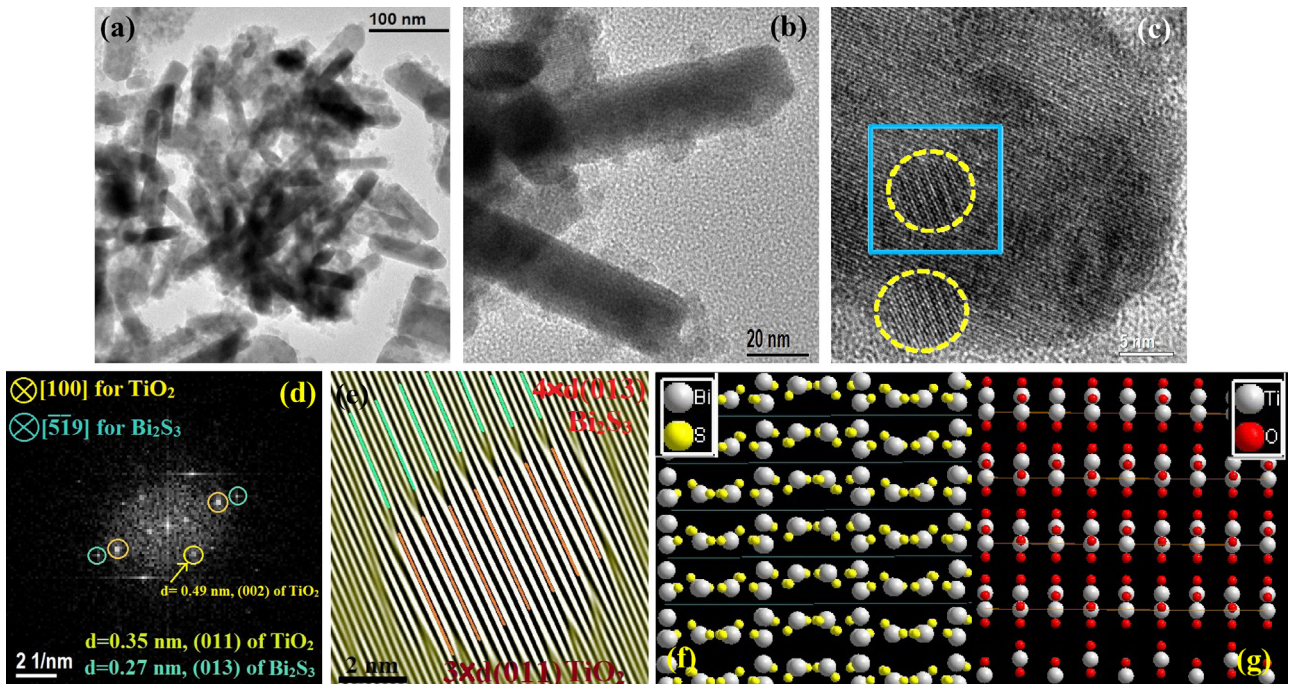
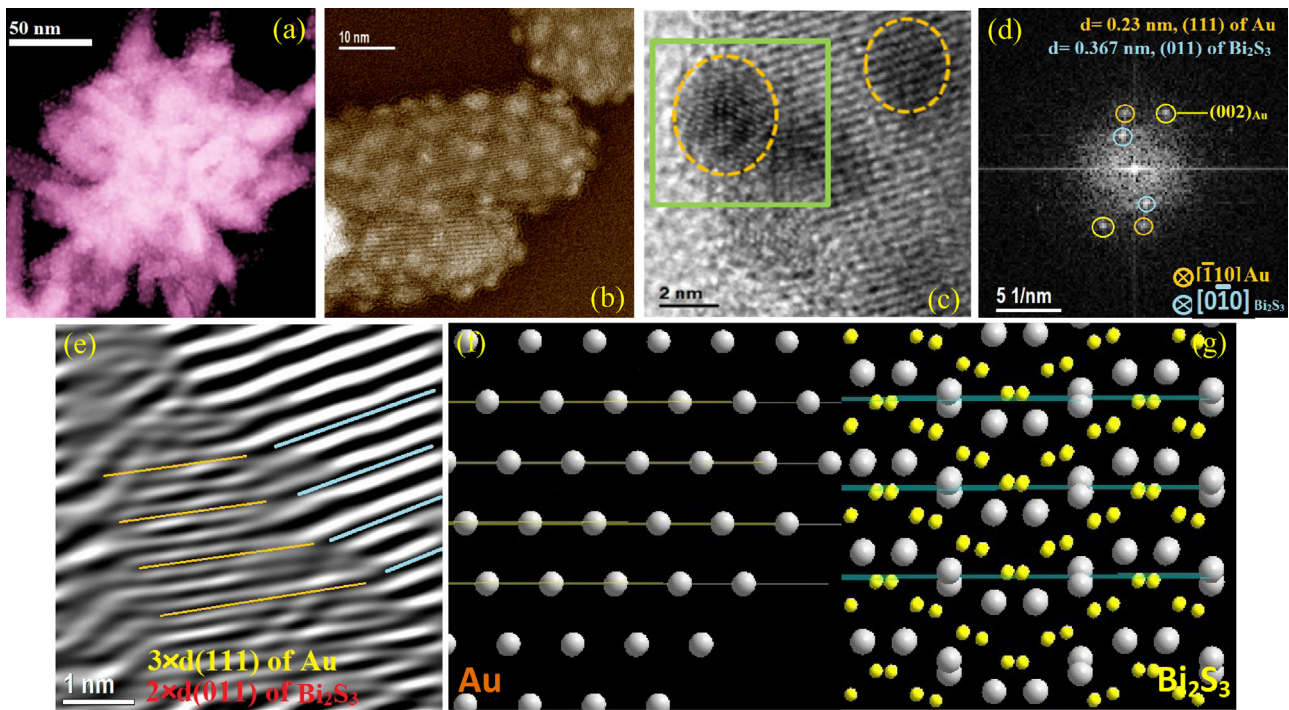


Fig. 3. (a) Large area TEM image of pure  $\text{Bi}_2\text{S}_3$  nanorod assembly. (b) A closer view of two nanorods assembly. (c) HRTEM image of one nanorod. (d) FFT pattern of yellow square area in (c). (e) Atomic arrangement of the nanorods. (For interpretation of the references to colour in this figure legend, the reader is referred to the web version of this article.)



**Fig. 4.** (a) TEM image of NHS2. (b) A closer view of a nanorods decorated with a number  $\text{TiO}_2$  nanoparticles. (c) HRTEM image of the nanorods with two  $\text{TiO}_2$  nanoparticles showing by yellow circles. (d) FFT pattern of the blue square region. (e) Reconstructed HRTEM image shows that  $\text{Bi}_2\text{S}_3$  (013) plane and  $\text{TiO}_2$  (011) plane along the same direction. (f)–(g) Atomic model of  $\text{Bi}_2\text{S}_3$  and  $\text{TiO}_2$  showing same direction of growth. (For interpretation of the references to colour in this figure legend, the reader is referred to the web version of this article.)



**Fig. 5.** (a) Dark field TEM image of Au decorated  $\text{Bi}_2\text{S}_3$  nanorod assembly. (b) Closer view of nanorods assembly which shows two nanorods with uniform Au decoration. (c) TEM image of a nanorod with 3–4 Au particle decoration. (d) FFT pattern of green squared area in (c). (e) Reconstructed HRTEM image showing same direction of growth of (111) plane of Au and (011) plane of  $\text{Bi}_2\text{S}_3$ . (f)–(g) Atomic model showing the matching of  $3 \times d(111)$  of Au and  $2 \times d(011)$  of  $\text{Bi}_2\text{S}_3$ . (For interpretation of the references to colour in this figure legend, the reader is referred to the web version of this article.)

at  $399\text{ cm}^{-1}$  corresponds to  $\text{B}_{1g}$  vibrational mode caused by symmetric bending vibration of O-Ti-O and  $516\text{ cm}^{-1}$  corresponds to  $\text{A}_{1g}$  vibrational mode arising due to antisymmetric bending vibration. The Raman spectra of  $\text{Bi}_2\text{S}_3/\text{TiO}_2$  composites consist of both Raman peaks of  $\text{Bi}_2\text{S}_3$  and  $\text{TiO}_2$  phases. It is very interesting that

the Raman spectra of  $\text{Bi}_2\text{S}_3/\text{TiO}_2$  heterostructures contain a small peak around  $123\text{ cm}^{-1}$  and the peak at  $237\text{ cm}^{-1}$  becomes more prominent. The peak at  $123\text{ cm}^{-1}$  is not a Raman active mode but an IR active phonon mode ( $\text{B}_{3u}$ ). In general IR active mode does not appear in Raman spectrum but this IR-active to Raman-active

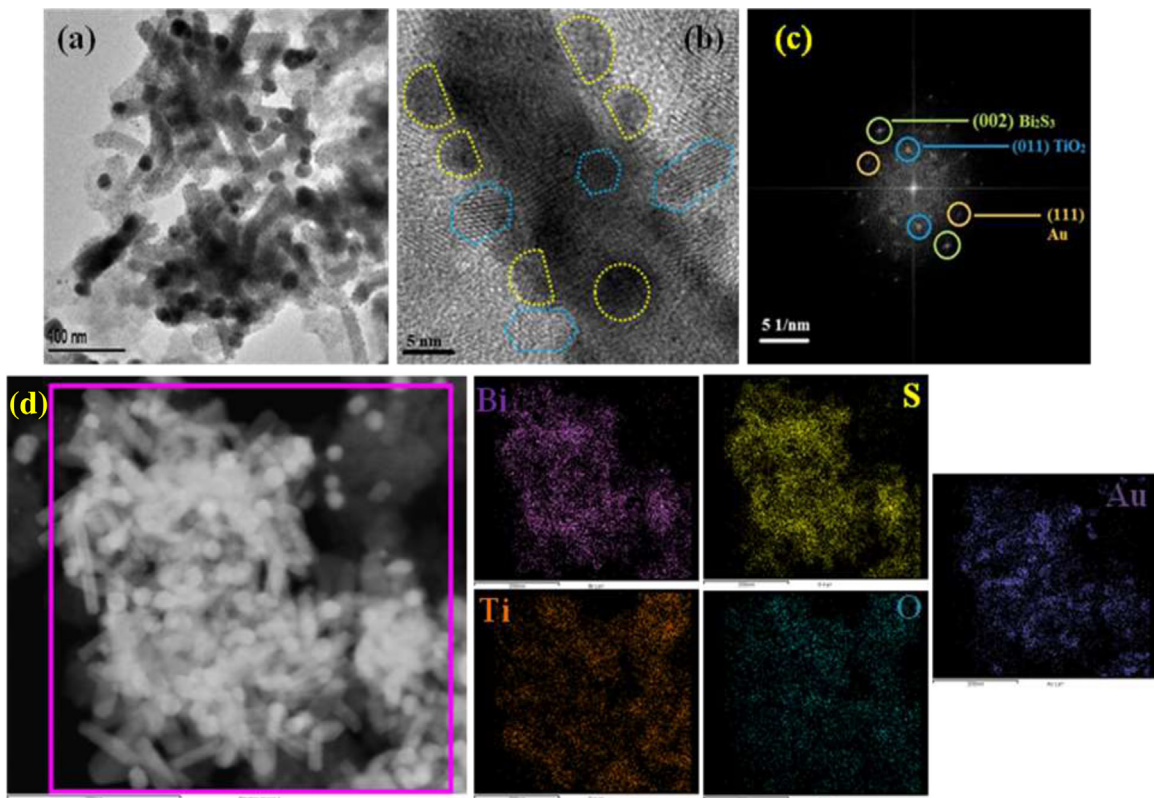


**Fig. 6.** TEM image of two nanorods assembly decorated with both  $\text{TiO}_2$  and Au nanoparticles. (b) HRTEM image showing a  $\text{Bi}_2\text{S}_3$  nanorod with a number of Au (yellow color) and  $\text{TiO}_2$  (blue color) particle decoration. (c) FFT pattern shows the presence of three phases  $\text{Bi}_2\text{S}_3$ ,  $\text{TiO}_2$  and Au. (d) EDS elemental mapping over two assemblies. (For interpretation of the references to colour in this figure legend, the reader is referred to the web version of this article.)

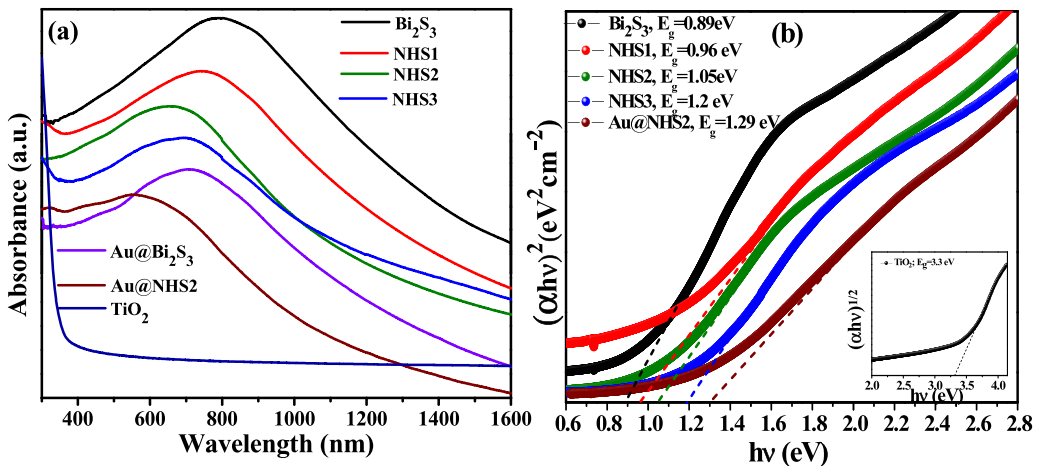


**Fig. 7.** (a) Absorbance spectra of pure  $\text{Bi}_2\text{S}_3$ , pure  $\text{TiO}_2$  and their nanoheterostructures. Absorbance edge of  $\text{Bi}_2\text{S}_3$  shifts towards lower wavelength on heterostructure formation. (b) Tauc plot of different samples showing change of band gap. Inset shows indirect band gap of anatase  $\text{TiO}_2$ .

transition occurs generally due to breaking of symmetry in the nanostrucrure material due to random displacement of defects in the lattice [35]. An interesting observation we get from the Raman spectrum is that  $E_g$  peak of  $\text{TiO}_2$  at  $148 \text{ cm}^{-1}$  gradually shifts to higher wavenumber. However,  $E_g$  peak at  $645 \text{ cm}^{-1}$  shifts towards lower wavenumber. It indicates that there must be an interaction between  $\text{Bi}_2\text{S}_3$  and  $\text{TiO}_2$  and the crystalline defect states of  $\text{TiO}_2$  are modified due to composite formation (as  $\text{TiO}_2$  is epitaxially connected to the  $\text{Bi}_2\text{S}_3$  which will be discussed in the TEM analysis section). The crystalline defects can change the vibrational mode of  $\text{TiO}_2$ , it can act as a trap to capture photo generated electron resulting in an electron–hole separation which is beneficial for photo-

tocatalytic activity. We also notice that the intensity of both  $\text{TiO}_2$  and  $\text{Bi}_2\text{S}_3$  drastically decreases and broadens for the composites. This can be a result of scattering loss due to defects formation at the interface between  $\text{Bi}_2\text{S}_3$  and  $\text{TiO}_2$ , especially the  $E_g$  peak of  $\text{TiO}_2$  at  $148 \text{ cm}^{-1}$  is present in all the composites but it is broadened and blue shifted. The  $E_g$  mode of  $\text{TiO}_2$  associated with O–O interactions which makes it more sensitive to make oxygen vacancy [36]. Lattice defect such as the removal of an oxygen atom from its lattice position makes the bond weak and shifts the neighboring titanium atom to their mean position and as a result of it the band is blue shifted [37]. Specifically, the band broadening and shifting to higher wavenumber is associated with lattice contraction which is a result

of oxygen vacancy formation [38]. The oxygen vacancy formation of the  $\text{Bi}_2\text{S}_3/\text{TiO}_2$  heterostructure was confirmed from XPS analysis. An XPS spectrum of O 1s (SI, Fig. S2b) was resolved into three peaks at 530.5 eV, 532.9 eV and 533.8 eV respectively. The peak at 530.5 eV arises due to Ti-O bond formation and on the other hand the other two peaks correspond to oxygen vacancy or defects and chemically adsorbed species such as  $\text{H}_2\text{O}$  [39]. The relative intensity of the peak at 533.8 eV related to chemically adsorbed  $\text{H}_2\text{O}$  is too low compared to the other peaks. Hence the contribution of  $\text{H}_2\text{O}$  molecules is negligible. The peaks at 459.2 eV and 465 eV correspond to the XPS peaks of  $\text{Ti} 2\text{p}_{3/2}$  and  $\text{Ti} 2\text{p}_{5/2}$  respectively for anatase  $\text{TiO}_2$  (SI, Fig. S2c). Each peak can be resolved into two peaks which suggest the presence of both  $\text{Ti}^{4+}$  and as well as  $\text{Ti}^{3+}$  state. Thus we can conclude that direct contact between  $\text{TiO}_2$  and  $\text{Bi}_2\text{S}_3$  modifies the surface states of both  $\text{Bi}_2\text{S}_3$  and  $\text{TiO}_2$ .

### 8.1. TEM analysis

Fig. 3a shows the large area TEM image of as-synthesized nanourchin of pure  $\text{Bi}_2\text{S}_3$  by colloidal process. The nanourchins are  $\sim 200 \pm 20$  nm in size with monodisperse in nature and good colloidal stability in organic solvent. Closer view of two nanourchins in Fig. 3b demonstrates self assembly of nanorods. Fig. 3c and Fig. 3d shows the HRTEM and FFT pattern of a typical type nanorod. From the FFT pattern, we have assigned the plane as (5/201) with d-spacing 0.4 nm, (212) with d-spacing 0.27 nm and (011) with d-spacing 0.36 nm when viewed along  $\sim [5\bar{1}9]$  zone axis. The main reason for growth along [5/201] direction is again presence of a permanent dipole along this direction for alternative array of 2- S rich layer and 1- Bi rich layer. For this case, after the nucleation  $\text{Bi}_2\text{S}_3$  nuclei might grow along polar direction [011] and [5/201]. The (5/201) plane is S-rich and undergoes stabilisation by  $\text{NH}_2$ -group of OLAM by electron donation of amine to sulphur empty shell. Atomic arrangement of Bi and S under  $[5\bar{1}9]$  zone axis is shown in Fig. 3e. We have identified that some of the  $\text{Bi}_2\text{S}_3$  nanorods were grown along another zone axis [010]. Fig. S3a and Fig. S3b shows the HRTEM image and the corresponding FFT pattern of a single nanorod respectively. Two perpendicular planes with d-spacing value 0.52 nm and 0.37 nm were identified as (200) and (011) planes.

To get more inside for formation mechanism we have varied the reaction condition especially the ratio of two capping agents. The decomposition of  $\text{Bi}(\text{S}_2\text{CNEt}_2)_3$  in pure OLAM in presence of 1-dodecanthiol (1-DDT) (no oleic acid) results in the formation of only  $\text{Bi}_2\text{S}_3$  nanorods (SI, Fig. S4a) with poor size distribution and variable aspect ratio. Use of 0.5 ml oleic acid (OA) with fixed amount of OLAM and 1-DDT favors the formation of some  $\text{Bi}_2\text{S}_3$  nanorod assembly but complete 3D nature is not there (SI, Fig. S4b). We have found that with increase of OA concentration, the assembly size gradually increases and a complete 3D urchin like morphology can be achieved (SI, Fig. 4f). With controlling the amount of OA we can control nanourchin size from 150 nm to 500 nm. Increase of OLAM concentration (in absence of OA) decreases the nanorod size. So OLAM here acts as nucleating agent to initiate the decomposition of  $\text{Bi}(\text{S}_2\text{CNEt}_2)_3$  complex and capping agent for specific Bi and S rich polar facets but do not play a crucial role in assembly formation. Use of OA results in a limited ligand protection on the surface of nanorods. The formation of amide bond by reaction between amine group of OLAM and acid group of OA at reaction temperature might decrease the capping efficiency of OLAM which accelerates the hierarchical shape formation [40–42].

Fig. 4a depicts the TEM images of  $\text{Bi}_2\text{S}_3/\text{TiO}_2$  NHS2 (at Bi: Ti = 1: 1.33) where nanourchin is found to be decorated with  $\text{TiO}_2$  nanocrystals. Large area TEM image [in SI, Fig. S5] shows that each of nanourchins is well decorated with  $\text{TiO}_2$  NCs. Closer view in Fig. 4b over 2–3 nanorods demonstrate that each nanorod is decorated

with multiple number of  $\text{TiO}_2$  nanocrystals. The low contrast of  $\text{TiO}_2$  NCs might be for low thickness of NC and lower Z value than that of  $\text{Bi}_2\text{S}_3$ . Fig. 4c shows the HRTEM image of the tip area of nanorod where two  $\text{TiO}_2$  NCs are situated. Fig. 4d shows the FFT pattern obtained from the blue colored square area of Fig. 4c. The spots appearing in FFT originate from the planes of both  $\text{Bi}_2\text{S}_3$  and  $\text{TiO}_2$  phases. The d-values obtained from two yellow circled spots are 0.49 nm and 0.35 nm which are assigned as (002) and (011) plane of  $\text{TiO}_2$  respectively. The calculated zone axis for viewing  $\text{TiO}_2$  NCs is [100]. The zone axis for  $\text{Bi}_2\text{S}_3$  is  $[5\bar{1}9]$  which was also assigned same as for pure  $\text{Bi}_2\text{S}_3$  nanorods. The d-value obtained from cyan color spot which is also along the same direction of (011) plane of  $\text{TiO}_2$  is found to 0.27 nm, which is the reflection of (013) plane of  $\text{Bi}_2\text{S}_3$ . The growth of (011) plane of  $\text{TiO}_2$  along the same direction of (013) of  $\text{Bi}_2\text{S}_3$  is an indication of epitaxy between these two planes. Fig. 4e shows the reconstructed HRTEM image by masking the two highlighted spots in Fig. 4d which also clearly shows the epitaxy along the [013] direction of  $\text{Bi}_2\text{S}_3$  NRs. The cyan and red colored lines are indicated for the  $\text{Bi}_2\text{S}_3$  and  $\text{TiO}_2$  parts respectively for better visibility of coincidence of planes. Although the large d-value difference in between (011)  $\text{TiO}_2$  and (013)  $\text{Bi}_2\text{S}_3$  is there. So, large lattice mismatch is present if one compare the matching of one (011) plane with (013) plane. But the reconstructed HRTEM revealed that periodic arrangement of  $4 \times d(013)$  ( $= 1.08$  nm) of  $\text{Bi}_2\text{S}_3$  matches exactly with  $3 \times d(011)$  ( $= 1.05$  nm) of  $\text{TiO}_2$  which results in minimum lattice mismatch between  $\text{Bi}_2\text{S}_3$  and  $\text{TiO}_2$ . Fig. 4f and g shows an atomic arrangement of (011) plane of  $\text{TiO}_2$  and (013) planes of  $\text{Bi}_2\text{S}_3$  and the match between 3d(011) and 4d(013) planes (Fig. 4e). The  $\text{TiO}_2$  NCs which are situated at the side surface can also be related by above established epitaxial relationship (SI, Fig. S6a and b). The perpendicular facet of {013} of  $\text{Bi}_2\text{S}_3$  is S-rich. So deposition of  $\text{Ti}^{4+}$  along with this facet is highly feasible for formation of strong covalent Ti-S bond. Atomic arrangement in Fig. 4f and g shows the position of different atoms at heterojunction.

The Bi:Ti ratio was varied to get different type of heterostructure to maximise the photocatalytic activity of heterostructure. Each nanorod is decorated with 2–3  $\text{TiO}_2$  NCs for Bi:Ti = 1:0.5. Excellent epitaxy has been confirmed from HRTEM (SI, Fig. S7b). Free  $\text{TiO}_2$  NCs are formed for higher molar ratio, Bi: Ti = 1:4 instead of epitaxial growth on  $\text{Bi}_2\text{S}_3$ . Inverted HRTEM image clearly shows the presence of both epitaxially connected and free standing  $\text{TiO}_2$  onto  $\text{Bi}_2\text{S}_3$  nanorod (SI, Fig. S7d).

Fig. 5a shows the STEM-DF image of Au NC homogeneously decorated on  $\text{Bi}_2\text{S}_3$  nanourchin. Fig. 5b shows the closer view of 2–3 nanorods where multiple number of Au NCs with size  $\sim 3$  – 5 nm are situated on the surface. No free standing Au NCs were found due to the Au-S eternal affinity. HRTEM image in Fig. 5c shows the co-existence of lattice fringes both from Au and  $\text{Bi}_2\text{S}_3$ . Fig. 5d shows the FFT pattern from the green square area of Fig. 5c. We assigned the zone axis for  $\text{Bi}_2\text{S}_3$  as [010] and for Au as [110]. We identified the (002) and (111) planes from orange and yellow circled spots. Epitaxial growth of (111) plane of Au over (011) plane of  $\text{Bi}_2\text{S}_3$  nanorods is established from FFT analysis. Reconstructed TEM image (using Gatan Software) by masking the circular spots in FFT shows the epitaxial relationship between Au and  $\text{Bi}_2\text{S}_3$  in Fig. 5e. Periodic arrangement of  $3 \times d(111)$  ( $= 0.69$  nm) of Au matches closely with  $2 \times d(011)$  ( $= 0.72$  nm) of  $\text{Bi}_2\text{S}_3$ . Fig. 5f and g show the atomic arrangement of (111) plane of Au and (011) plane of  $\text{Bi}_2\text{S}_3$  and the matching between 3d(111)Au and 2d(011)  $\text{Bi}_2\text{S}_3$  planes.

Fig. 6a illustrates the TEM image of  $\text{Bi}_2\text{S}_3/\text{TiO}_2/\text{Au}$  NHSs. Each of  $\text{Bi}_2\text{S}_3$  nanorods are found to be decorated with both  $\text{TiO}_2$  and Au nanocrystals. Fig. 6b depicts the HRTEM image of single nanorod decorated with multiple  $\text{TiO}_2$  and Au NCs. The highest contrast NCs are Au NCs (high Z value, marked with yellow circles) and lighter contrast NCs are  $\text{TiO}_2$  (cyan circled). Au NCs are found to be

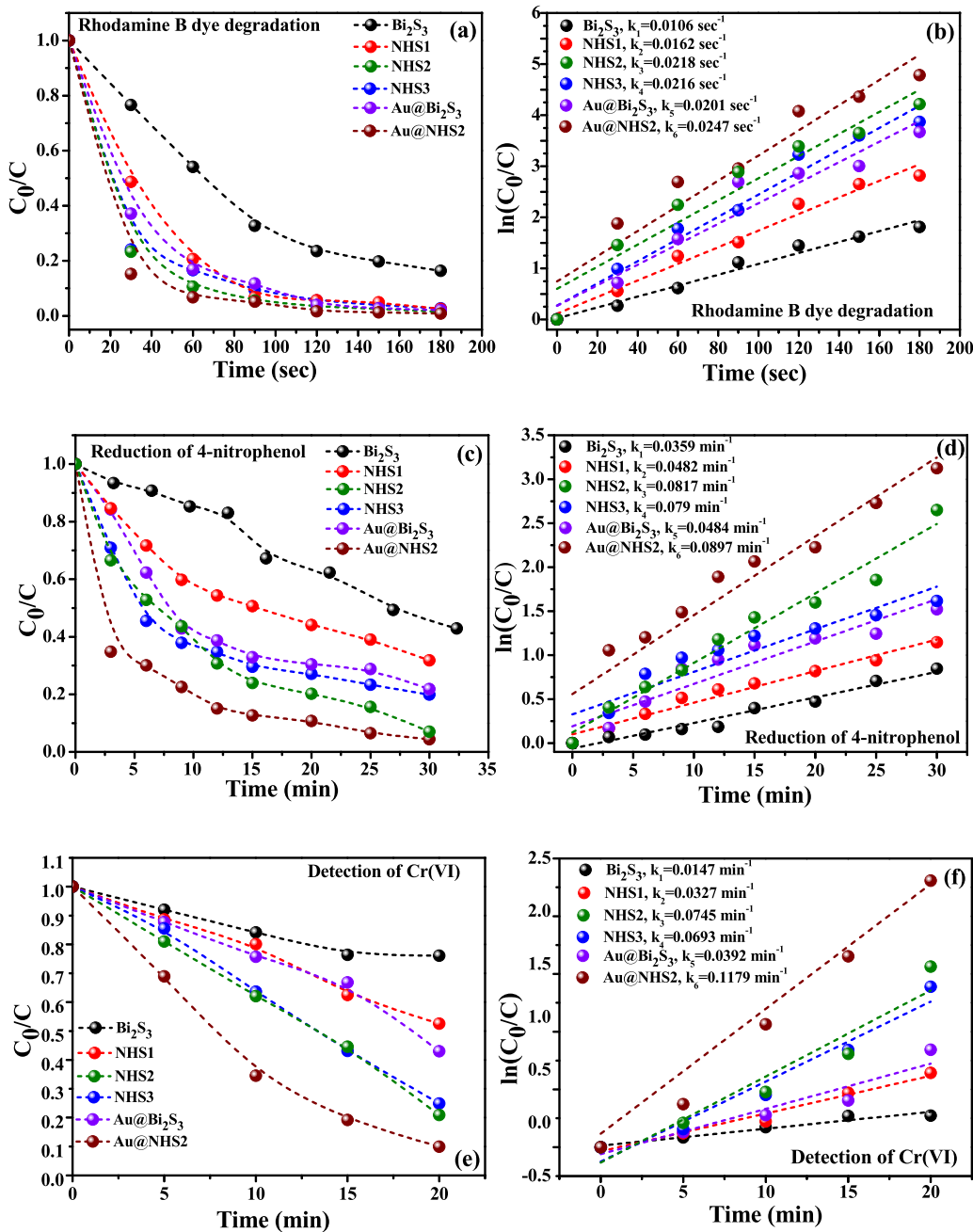


**Fig. 8.** Solar light driven (a)–(b) photo degradation of RhB dye. (c)–(d) photoreduction of 4-nitrophenol. (e)–(f) detection of Cr(VI).

solely grown onto Bi<sub>2</sub>S<sub>3</sub> facets without any direct contact with TiO<sub>2</sub> NCs. The characteristic planes of Au (111) and TiO<sub>2</sub> (011) obtained from FFT pattern in Fig. 6c confirm the formation of Au and TiO<sub>2</sub> NCs on Bi<sub>2</sub>S<sub>3</sub> nanorods. Fig. 6d shows the EDS element mapping over two Au and TiO<sub>2</sub> decorated Bi<sub>2</sub>S<sub>3</sub> nanourchin heterostructures which proves homogenous distribution of respective elements on the nanourchins.

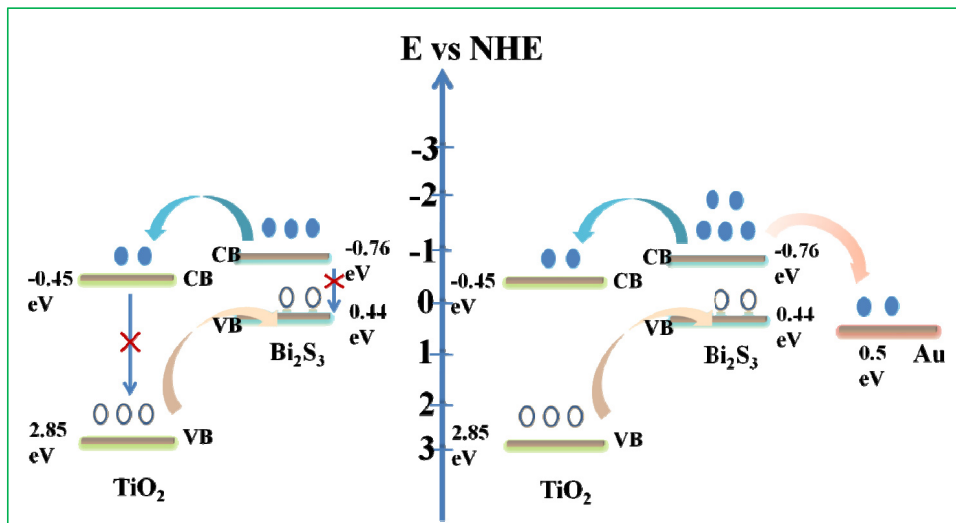
## 8.2. Optical properties

Room temperature UV-vis absorption spectra of Bi<sub>2</sub>S<sub>3</sub> nanorod assembly, pure TiO<sub>2</sub> nanoparticles and Bi<sub>2</sub>S<sub>3</sub>/TiO<sub>2</sub> heterostructures in the absence and presence of Au nanoparticles are shown in Fig. 7a. A strong absorption peak centered around 800 nm is observed for pure Bi<sub>2</sub>S<sub>3</sub> nanorod assembly. The absorbance feature covers the visible region and extended up to NIR region (~1600 nm)

of solar spectrum. The UV-vis absorption spectra of as synthesized TiO<sub>2</sub> exhibited an absorption peak at 370 nm which is the characteristic band edge absorption of anatase TiO<sub>2</sub> phase. The band edge absorption of Bi<sub>2</sub>S<sub>3</sub> is blue shifted from 800 nm to 564 nm on heterostructure formation. The band gaps of the as synthesized samples were calculated using the equation

$$(\alpha h\nu)^n = C (h\nu - E_g) \quad (1)$$

Where  $\alpha$ ,  $h$ ,  $\nu$  and  $E_g$  are the optical absorption coefficient, Planck constant, photon frequency and band gap of semiconductor, respectively and  $C$ ,  $n$  are constants. The value of 'n' depends upon whether the semiconductor is direct ( $n=2$ ) or indirect ( $n=1/2$ ) semiconductor. The indirect band gap of TiO<sub>2</sub> was calculated to be 3.3 eV (Fig. 7b inset). Sensitization of Bi<sub>2</sub>S<sub>3</sub> nanorod assembly with TiO<sub>2</sub> nanoparticles extended the absorption spectra from UV to visible range up to 1500 nm. From the Tauc plot shown in Fig. 7b, the band



**Scheme 1.** Relative band alignment of  $\text{Bi}_2\text{S}_3/\text{TiO}_2$  heterostructure and Au decorated  $\text{Bi}_2\text{S}_3/\text{TiO}_2$  nanoheterostructure.

gap of NHS increases from 0.89 eV to 1.2 eV with increasing of  $\text{TiO}_2$  content.  $\text{Bi}_2\text{S}_3/\text{TiO}_2$  heterostructure is a type II heterostructure. The electron is delocalized through the entire system as its low effective mass and the small conduction band offset of 0.31 eV [43,21]. Moreover  $\text{TiO}_2$  has a higher electron affinity of 5.1 eV than that of  $\text{Bi}_2\text{S}_3$  (electron affinity 4.58 eV) [44,19]. Therefore the electrons are delocalized towards  $\text{TiO}_2$  in the heterostructure. In contrast hole is more confined to  $\text{Bi}_2\text{S}_3$  as the higher effective mass and higher valance band offset of 2.06 eV [43,21]. Due to type II heterostructure formation and lower effective hole mass of  $\text{TiO}_2$ , holes are transferred to the  $\text{Bi}_2\text{S}_3$  nanorods [45]. In our asymmetric heterostructure, the electrons and holes have a different level of confinement. Here electrons gain a 0-D characteristic as the electrons are transferred to spherical  $\text{TiO}_2$  nanoparticle and the hole maintains a 1-D characteristic due to confined into the  $\text{Bi}_2\text{S}_3$  nanorods assembly. Thus the heterostructure formation offers a different dimensionality of electrons and holes [46]. Thus the band gap absorption of  $\text{Bi}_2\text{S}_3$  is blue shifted due to different level of confinement of electrons and holes in the heterostructure [47].

$\text{Au@Bi}_2\text{S}_3$  has an absorption band around 695 nm with a shoulder around 500 nm which arises due to Au nanoparticle ( $\sim 5$  nm) decorated on the nanorods assembly. The LSPR peak of Au nanoparticles is very sensitive to size, shape and the surrounding environment. Here the absorption peak due to LSPR of Au nanoparticles is not as prominent as the sizes of the Au nanoparticles are small to exhibit a proper LSPR absorbance. Epitaxially grown metal–semiconductor heterostructure gives rise to lower potential barrier and large overlap of electronic wave functions between  $\text{Bi}_2\text{S}_3$  and Au. As a result of these, photoexcited electrons in  $\text{Bi}_2\text{S}_3$  are transferred into interfacial states and reduce the absorbance of  $\text{Bi}_2\text{S}_3$  consistent with earlier reported results [48].

### 8.3. Photocatalytic activity

In order to evaluate the photocatalytic activity of all the as-synthesized, RhB was used as a model dye under artificial solar light irradiation (Fig. S8a). The photocatalysis of RhB is negligible in absence of any sample. Although the degradation of RhB is fast in presence of pure  $\text{Bi}_2\text{S}_3$  nanourchin (under solar light irradiation) but degradation in presence of pure  $\text{TiO}_2$  NCs (4–5 nm) is very slow.  $\text{TiO}_2$  took more than 2 h to complete degrade RhB. Nearly 75–80% RhB was found to be degraded in presence of  $\text{Bi}_2\text{S}_3$  nanourchin just in 3 min. The rate is found to be higher than the previous reported  $\text{Au-Bi}_2\text{S}_3$  metal semiconductor heterostructure. [28]

The enhanced reaction rate observed for pure nanourchin may be due to the increased surface area of hierarchical structures. The other nanourchins having size higher than 200 nm shows little slower photocatalytic activity probably for increase in mass of each assembly results faster sedimentation from solution before complete dye degradation. Fig. 8a shows the change of relative dye concentration in presence of different photo catalyst under white light irradiation. As the degradation was very fast, we took the aliquot in 30 s interval from the time light exposing. Initial reaction steps of all systems showed pseudo first order rate kinetics with time ( $t$ ), so degradation rate constant ( $k$ ) can be obtained from the linear fit of:  $\ln(C/C_0) = -kt$ , where  $C_0$  and  $C$  are initial and equilibrium dye concentration at time  $t$  respectively. Fig. 8b shows the all the experiments have been done under same power density of light ( $0.65 \text{ mW/cm}^2$ ). So simply comparing the  $k$  values we can compare the photocatalytic activity of different samples. Nanoheterostructures which are the composites of  $\text{TiO}_2$  and  $\text{Bi}_2\text{S}_3$  shows higher photocatalytic activity than pure  $\text{Bi}_2\text{S}_3$  nanourchin. Nearly 95–98% RhB is found to be degraded in presence of NHS1, NHS2 and NHS3 ( $\text{Bi}_2\text{S}_3/\text{TiO}_2$  heterostructures with a Bi:Ti ratio 1:0.5, 1:1.33, 1:4 respectively). Maximum rate constant is found for NHS2 ( $k_3 = 0.0218 \text{ s}^{-1}$ ; Bi:Ti = 1:1.33). The rate constant value is more than double of pure  $\text{Bi}_2\text{S}_3$  nanourchin. Increase of  $\text{TiO}_2$  concentration improves the value of rate constant. But for NHS3, a little decrease of  $k$  value is obtained. Small Au NCs decorated  $\text{Bi}_2\text{S}_3$  nanourchins also shows an enhancement of photocatalytic acitivity than pure  $\text{Bi}_2\text{S}_3$ . The obtained  $k$  value for  $\text{Au@Bi}_2\text{S}_3$  NHS is just twice that of pure  $\text{Bi}_2\text{S}_3$  sample. The increase of photocatalytic activity in case of NHS might be attributed to unique nanorod/nanocrystal epitaxial heterostructure and the improved charge separation process. In order to understand the mechanism we studied the relative band alignment of  $\text{Bi}_2\text{S}_3$ ,  $\text{TiO}_2$  and Au. The band alignment of heterostructure is shown in Scheme 1. According to previous report, the conduction band position of  $\text{TiO}_2$  is lower than that of  $\text{Bi}_2\text{S}_3$ . Whereas the valence band of  $\text{Bi}_2\text{S}_3$  position is much higher than that of  $\text{TiO}_2$  which results in a type-II band alignment. The effective charge carrier separation inside the heterostructure depends upon the relative migration rates of electrons and holes in each semiconductor. We calculated the diffusion time of photo generated charge carriers inside both the semiconductors using the following equation for charge carrier diffusivity ( $D$ ):

$$D = \frac{\mu k_B T}{q_e} \quad (2)$$

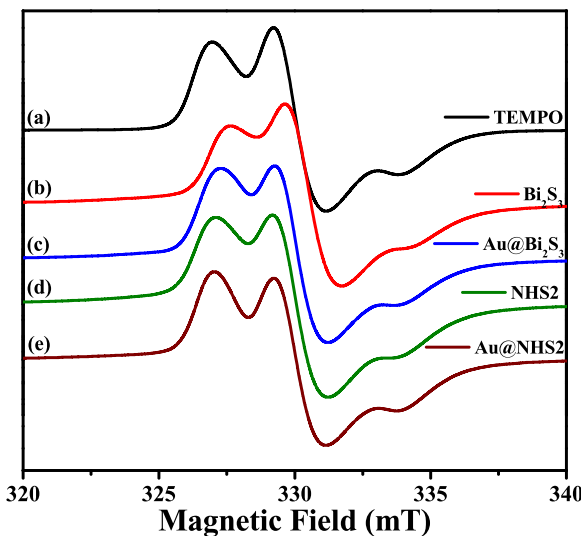


**Fig. 9.** The ESR signal of (a) 0.02 mM TEMPO in toluene and (b)–(e) in presence of 0.1 mg/mL of  $\text{Bi}_2\text{S}_3$ ,  $\text{Au}@\text{Bi}_2\text{S}_3$ ,  $\text{NHS2}$  and  $\text{Au}@\text{NHS2}$  respectively after 10 min of irradiation.

where  $\mu$  is the mobility of charge carriers,  $k_B$  is Boltzmann coefficient,  $T$  is the absolute temperature, and  $q_e$  is the charge of the electron. The diffusivities of photogenerated electrons and holes inside  $\text{TiO}_2$  crystal are calculated to be  $1 \times 10^{-6} \text{ m}^2/\text{s}$  and  $4 \times 10^{-5} \text{ m}^2/\text{s}$  respectively taking the mobility value of electrons and holes as  $4 \times 10^{-5} \text{ m}^2/\text{Vs}$  and  $1.6 \times 10^{-3} \text{ m}^2/\text{Vs}$  respectively at 300 K [45]. The time required for the migration of charge carriers from the centre of  $\text{TiO}_2$  NCs to the interface region between  $\text{TiO}_2$  and  $\text{Bi}_2\text{S}_3$  can be determined by the formulae:

$$\tau = \frac{r_0^2}{\pi^2 D} \quad (3)$$

where  $r_0$  is the migration length, which is taken as 2.5 nm ( $\text{TiO}_2$  NCs size  $\sim 5\text{--}6$  nm). So the calculated migration time of electron and hole are 0.6 picosec and 0.02 picosec respectively. So faster migration of hole compare to electron (nearly 30 times faster) is expected from the inside of  $\text{TiO}_2$  NCs which results in relatively high electron density inside the  $\text{TiO}_2$  NCs and large hole concentration at NC surface or at the interface. So hole migration is expected from  $\text{TiO}_2$  to  $\text{Bi}_2\text{S}_3$  nanorods.

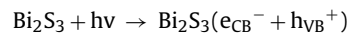
In similar process we have calculated the migration time for photogenerated carriers of  $\text{Bi}_2\text{S}_3$  nanorods. Mobility values of electrons and holes of  $\text{Bi}_2\text{S}_3$  were taken as  $0.35 \text{ m}^2/\text{Vs}$  and  $0.08 \text{ m}^2/\text{Vs}$  respectively. [49] For an 1-D nanostructure, carriers from the centre of nanorod can migrate in two perpendicular direction: migration along the width and length. As most of the  $\text{TiO}_2$  NCs are situated onto side surfaces of  $\text{Bi}_2\text{S}_3$  nanorods, we calculated the migration time along the width only. The migration time for electron and hole from centre of nanorods is found to be 0.07 fsec and 2.4 fsec respectively. So photoexcited electrons in  $\text{Bi}_2\text{S}_3$  nanorods migrate much faster ( $\sim 35$  times) to the surface compare to hole in  $\text{Bi}_2\text{S}_3$ . So transfer of photoexcited electrons from  $\text{Bi}_2\text{S}_3$  to  $\text{TiO}_2$  is much more facile compare to hole transfer process. So, after the photoexcitation of  $\text{NHS}$ , complete charge separation is possible which leads to high concentration of hole in  $\text{Bi}_2\text{S}_3$  nanorods and electron rich  $\text{TiO}_2$ .

The above explanation was further verified experimentally by taking the room temperature PL spectra of pure and  $\text{NHS}$  samples. PL spectra can be utilized to investigate the recombination rate of the photogenerated electron–hole pairs. The decrease in the recombination rate gives rise to a low PL intensity [50–52]. Fig. S9 in SI shows the PL spectra. The intensities of characteristic emission peaks of  $\text{TiO}_2$  at 410 nm, 430 nm and 460 nm ascribed to mainly  $\text{Ti}^{3+}$

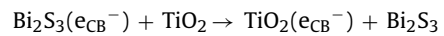
and oxygen vacancy defect states are found to be decreased with heterostructure formation which suggests improvement of charge separation.

The interface between  $\text{Bi}_2\text{S}_3$  and  $\text{Au}$  nanoparticles makes Schottky junction due to higher electron affinity (work function) of  $\text{Au}$ . The electric field across Schottky junction enhances e–h separation. [25,26] Photoexcited electrons in  $\text{Bi}_2\text{S}_3$  which transferred to the surface very fast, can move both to the epitaxially connected  $\text{TiO}_2$  NCs and  $\text{Au}$  NCs as demonstrated in Scheme-I. The photogenerated electrons on the surfaces of  $\text{TiO}_2$  and  $\text{Au}$  can react with surface absorbed oxygen molecules to produce superoxide radical anions ( $\cdot\text{O}_2^-$ ). The holes on the surface of  $\text{Bi}_2\text{S}_3$  can be transferred to the absorbed  $\text{H}_2\text{O}$  molecules to generate highly oxidising  $\text{OH}^\bullet$  radical according to the following redox steps:

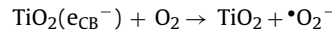
Charge separation



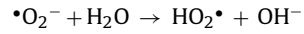
Charge transfer



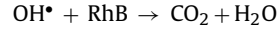
Superoxide radical ( $\cdot\text{O}_2^-$ ) formation



$\text{OH}^\bullet$  radical formation



Dye degradation



The formation of  $\text{OH}^\bullet$  radical as an active photocatalytic species during photocatalysis can be probed using terephthalic acid (TA). Reaction of TA with  $\text{OH}^\bullet$  radicals can generate fluorescent 2-hydroxyterephthalic acid (TAOH) which shows emission peak at 425 nm with excitation at 315 nm [50]. The fluorescence intensity of TAOH is proportional to the amount of  $\text{OH}^\bullet$  produced on the surface of photocatalysts. Fig. S10 in SI shows the emission of in-situ formed TAOH in water in presence of different photocatalyst when irradiated for 20 mins. Maximum fluorescence intensity of TAOH has been found for  $\text{Au}@\text{NHS2}$  which reveals that maximum  $\text{OH}^\bullet$  radical formation by  $\text{Au}@\text{NHS2}$  heterostructure at a fixed time of solar light irradiation.

We have also studied the photocatalytic reduction of 4-NP in presence of  $\text{NaBH}_4$ . The 4-NP shows absorbance peak at about 317 nm and it has been red shifted to 405 nm in presence of  $\text{NaBH}_4$  for formation of 4-nitrophenolate ion. Although  $\text{NaBH}_4$  is a strong reducing agent it cannot be capable of reducing 4-nitrophenolate in presence of solar light. Presence of catalyst (nanourchin or  $\text{NHSs}$ ) triggers the conversion of 4-nitrophenolate to 4-aminophenolate in presence of light irradiance. The depletion of the 4-nitrophenol peak at 400 nm and the concomitant increase of a peak at 297 nm has been monitored over time (SI, Fig. S8b). Fig. 8c shows different reduction concentration of 4-NP in presence of different photocatalyst under solar light irradiation. Fig. 8d shows catalytic rate constants obtained for different photocatalyst. The rate in presence of pure  $\text{Bi}_2\text{S}_3$  nanourchin is  $3.6 \times 10^{-2} \text{ min}^{-1}$  whereas that of the  $\text{Au}@\text{NHS2}$  i.e.  $\text{Bi}_2\text{S}_3/\text{TiO}_2/\text{Au}$  is  $9.0 \times 10^{-2} \text{ min}^{-1}$ . The photoexcited electrons in the semiconductors are responsible for the functional group transformation. After the photoexcitation as-generated holes undergoes neutralised by the hydrides ( $\text{H}^-$ )/electrons from  $\text{BH}_4^-$  and the electrons in CB can directly transfer to surface absorbed 4-nitrophenolate ion. Greater extent of formation of photoexcited charge carriers in  $\text{Au}@\text{NHS2}$  results in the highest photocatalytic reduction property.

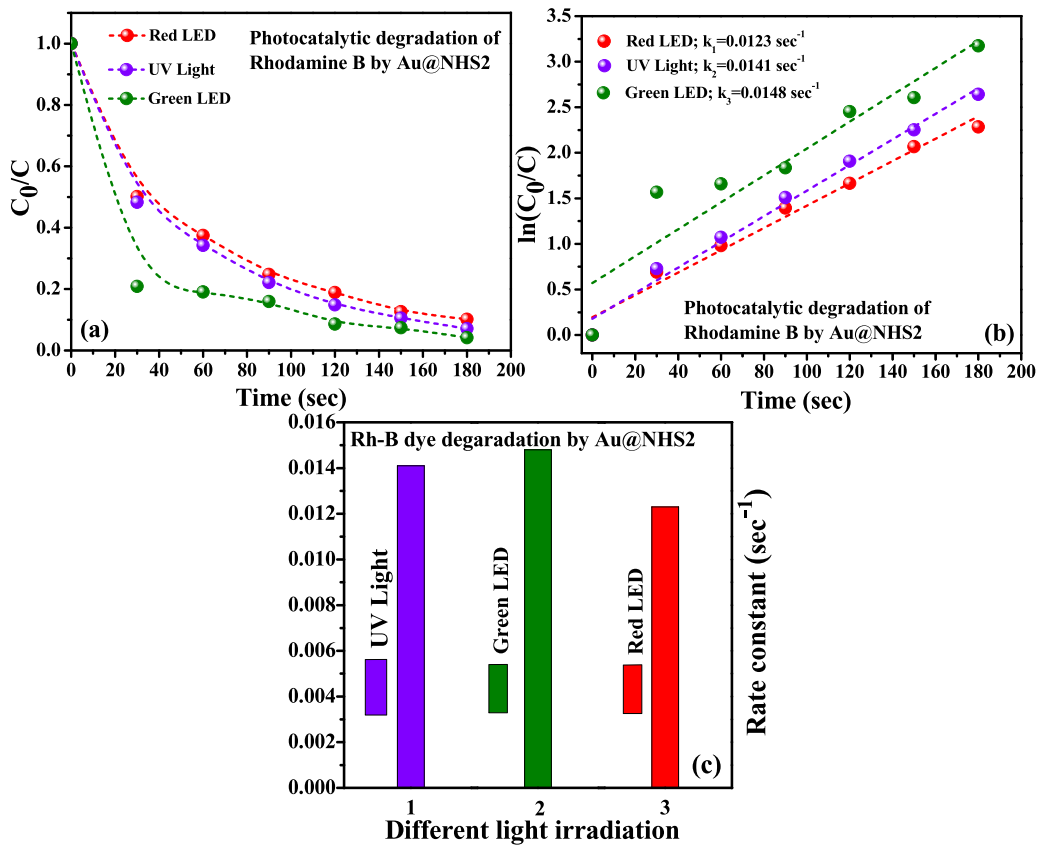
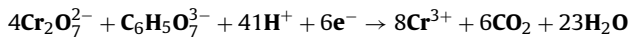


Fig. 10. (a)–(b) Photodegradation of Rh-B dye with UV and different LED lights. (c) Histogram plot of rate constant under different light irradiation.

Removal of toxic metal ions Cr(VI) from ground water is essential to get purified water. Reducing Cr(VI) to Cr(III), which is less toxic and easily precipitates under alkaline or neutral pH, is one of the promising ways to remove Cr(VI) toxicity from waste water. Citric acid has been used as hole scavenger. Fig. 8e and f shows the rate of Cr(VI) reduction in presence of different photocatalyst. Irradiation of Cr(VI) solution in presence of citric acid or in absence of any catalysis does not lead to any reduction of Cr(VI). Reduction kinetics has been monitored by absorbance spectroscopy with characteristic peak of Cr(VI) at 543 nm (SI, Fig. S8c). As-synthesized  $\text{Bi}_2\text{S}_3$  nanourchin shows good photocatalytic reduction of Cr(VI) with a rate constant of  $1.47 \times 10^{-2} \text{ min}^{-1}$ . The maximum rate constant is achieved for Au@NHS2 heterostructure with a rate constant of  $0.12 \text{ min}^{-1}$ , which is nearly 10 times higher than pure  $\text{Bi}_2\text{S}_3$ . The redox mechanism for conversion of Cr(VI) to Cr(III) can be expressed as follows:



Thus Cr contaminated wastewater can be purified by environmental friendly photocatalysis process.

The long term cycling stability is an essential requirement for its practical use in photocatalytic experiments. During the recycle experiments, Au@NHS2 were recollected and reused for five times for photocatalytic degradation shown in Fig. S11–S13 in supporting information. We have found that the rate constants ( $0.0247 \text{ s}^{-1}$ ) are same up to five cycles which proves that the as-synthesized system is a robust catalyst. For better understanding the photocatalytic activity of ternary heterostructure, we have performed photocatalytic experiment by using mixture of NHS2 and Au@ $\text{Bi}_2\text{S}_3$  to compare its catalytic activity with  $\text{Bi}_2\text{S}_3/\text{TiO}_2/\text{Au}$  ternary heterostructure. From Fig. S14 we have found that ternary

heterostructure has better rate constant ( $0.0247 \text{ s}^{-1}$ ) than that of the mixture of binary heterostructures ( $0.0225 \text{ s}^{-1}$ ) for RhB dye degradation. For the reduction of 4-paranitrophenol and detection of Cr(VI) we have similar results. Thus we can say that ternary heterostructure has better photocatalytic activity than that of the mixing of binary heterostructures.

### 8.3.1. Identifying the photoinduced electrons by ESR-spin label

Electron spin resonance (ESR) spectroscopy based on spin label TEMPO molecule is used to provide direct evidence of electron transfer under photoexcitation in  $\text{Bi}_2\text{S}_3$ , Au@ $\text{Bi}_2\text{S}_3$ , NHS2 and Au@NHS2. The unpaired electrons in TEMPO molecule generate strong ESR signals as illustrated in Fig. 9a recorded in toluene solution at 77 K [53]. The photogenerated electrons in semiconductors can reduce TEMPO to ESR silent hydroxyl amine (TEMPOH) [54,55]. Thus systematic observation of ESR signal intensity under identical experimental conditions with the addition of photocatalysts can demonstrate the photoinduced electron transfer from semiconductor to TEMPO molecule. The ESR spectra at 77 K of TEMPO were collected in the presence of  $\text{Bi}_2\text{S}_3$ , Au@ $\text{Bi}_2\text{S}_3$ , NHS2 and Au@NHS2 after 10 min of irradiation (Fig. 9b–e). The ESR spectra suggest that relative intensity of main peak at about 330 mT of TEMPO molecule is considerably damped with the addition of photocatalysts. Normally the free TEMPO radical does not react with oxidising species such as superoxide or holes and the systems before irradiation. Therefore damping of ESR signal is mainly associated with the generation of TEMPOH from TEMPO. The formation of TEMPOH clearly proves that electrons transfer from photoexcited semiconductor heterostructures to TEMPO molecule [56]. Moreover, ESR spectrum of Au@NHS2 is significantly damped indicating the best photocatalytic activity.

### 8.3.2. Beyond the maximum: plasmonic sensitization

As developed  $\text{Bi}_2\text{S}_3/\text{TiO}_2/\text{Au}$  ternary NHS shows excellent photocatalytic activity, the role of plasmonic absorbance of gold nanoparticles has been studied for better understanding and maximisation of photoactivity. For this purpose, wavelength dependent catalytic activity has been studied with UV and LED lamps irradiation including green (550 nm) and red (700 nm) with same irradiance intensity (optimised by a photometer). According to Fig. 10, maximum photocatalytic activity (RhB degradation) has been found with green LED excitation. As the plasmonic absorbance of Au nanocrystals (NCs) is in the green region of visible light so we can expect plasmon induced visible light activity of the material. For small spherical metal NCs where the far-field and near-field resonant frequency overlap completely, the highest near-field enhancement can be achieved when light is resonant with the Au NCs LSPR as they act as the concentrator of the local electric field. The optical absorbance mechanism of a semiconductor is described by Fermi's golden rule in electric dipole approximation. In semiconductor, the absorbance increases linearly with the intensity of the perturbation electric field. The near field enhancement can significantly enhance the inter-band or other optical transitions in the nearby semiconductor if the LSPR spectra overlap with them [57,58]. Absorbance spectra of  $\text{Au}@\text{NHS2}$  show a significant overlap of Au plasmonic absorbance and  $\text{Bi}_2\text{S}_3$  band gap absorbance. The enhancement of light absorbance can be estimated using the following equation [59]:

$$\text{FE} = \frac{\int_V dZ \int dx dy |\mathbf{E}(x, y, z)|^2}{\int_V dZ \int dx dy |\mathbf{E}_0|^2}$$

Where the integrating volume (V) refers to the volume in the semiconductor covered by the near-field.  $\mathbf{E}(x, y, z)$  is the value of the near-field at point  $(x, y, z)$ , and  $\mathbf{E}_0$  is the electric field of incident light. As the maximum area of  $\text{Bi}_2\text{S}_3$  nanorods are covered with Au NCs, V value is expected to be high. Thus the light absorption efficiency and also the rate of generation of e-h pair increases due to energy transfer through the near field enhancement. But we cannot conclude at this state, whether the direct electron transition from  $\text{Bi}_2\text{S}_3$  to Au or electric field enhancement due to plasmonic absorbance of Au plays the crucial role for high photoactivity.

For most plasmonic photocatalysis, metal nanoparticles serve as a sensitizer by greater utilization of the solar spectrum. By tailoring the size of the metal particles one can trigger the plasmon absorption from the visible to NIR region. Not only size but also the geometry affects the LSPR frequency as the asymmetry enables the electrons to resonate in more than one mode. Now to investigate the effect of near field enhancement we change the size and geometry of the Au nanoparticles. First of all we fabricate a 2-D array of Au NCs ( $\sim 10$  nm, SI, Fig. S16a) deposited over glass slide and a thin layer of non-conducting tetra-ethyl orthosilicate (TEOS) layer (5 nm) was deposited over Au NCs. NHS2 was deposited over TEOS to develop a sandwich device where direct transfer of carrier is not possible from metal to semiconductor or vice-versa. The device shows absorbance centered at 570 nm for Au LSPR absorbance (SI, Fig. S15a). Wavelength dependent photocatalytic activity study shows maximum activity can be obtained with green LED excitation shown in the SI, Fig. S17. Direct excitation of  $\text{TiO}_2$  (with UV light) and  $\text{Bi}_2\text{S}_3$  leads to poor catalytic activity. Here direct charge transfer between Au and  $\text{Bi}_2\text{S}_3$  is not possible as there is an insulating layer between them. The near field enhancement is solely responsible for greater photoactivity as excitation with green LED leads to direct excitation of Au nanoparticles. Another device has been developed in similar way with Au nanorods (TEM in SI, Fig. S16b). Where LSPR absorbance for longitudinal mode is found at 653 nm (SI, Fig. S15b) which is coupled with absorption spectra of

$\text{Bi}_2\text{S}_3$ . Excitation with red LED (700 nm) thus gives the maximum photoactivity (SI, Fig. S18).

So, from above experiments we can conclude that direct plasmonic excitation of Au NPs maximise the photoactivity of  $\text{Bi}_2\text{S}_3/\text{TiO}_2$  heterostructure. The photoactivity of  $\text{Au}@\text{NHS2}$  under the solar irradiance ( $k = 0.025 \text{ s}^{-1}$ ) was found to be higher than with green LED excitation ( $k = 0.014 \text{ s}^{-1}$ ). Under solar irradiance simultaneous excitation of  $\text{TiO}_2$ ,  $\text{Bi}_2\text{S}_3$  and Au plasmonic is possible. The metal nanoparticles absorb, intensify and direct the light to the semiconductors for more absorption and also enhance e-h pair formation by near field enhancement. Also we have successfully fabricated a visible light photocatalytic device to convert visible light energy to chemical energy with a 2D array of Au NPs or NRs as a near field enhancing layer. So we can conclude that not only heterostructure formation but also plasmon induced near field enhancement is potential for photocatalytic performance.

## 9. Conclusion

In summary, we have successfully synthesized high quality  $\text{Bi}_2\text{S}_3/\text{TiO}_2/\text{Au}$  nanoscale heterostructure, in which both  $\text{TiO}_2$  and Au NCs are epitaxially grown on the surface of  $\text{Bi}_2\text{S}_3$  nanorods. We found that oleic acid plays a crucial role for the formation of nanorod assembly of  $\text{Bi}_2\text{S}_3$  urchin morphology. Epitaxial interface of semiconductor-semiconductor and semiconductor-metal and proper band alignment of individual component favor the separation of electron-hole pair. The best photocatalytic activity is achieved for a particular Bi: Ti ratio i.e. 1:1.33. Absorption of light over a wide wavelength region, transportation of photo generated electrons and holes and creation of high near field through the plasmonic excitation improve the photocatalytic degradation of RhB, reduction of 4-nitrophenol and removal of Cr(VI) from water. Solid state device consisting of low and high band gap semiconductors and plasmonic metals can be used for efficient and echo friendly removal of pollutants in wastewater.

## Acknowledgment

The authors S. Paul and D. Barman acknowledge DST-INSPIRE fellowship and CSIR, India for providing the fellowship during the tenure of work.

## Appendix A. Supplementary data

Supplementary data associated with this article can be found, in the online version, at <http://dx.doi.org/10.1016/j.apcatb.2017.07.057>.

## References

- [1] J. Li, S.K. Cushing, P. Zheng, T. Senty, F. Meng, A.D. Bristow, A. Manivannan, N. Wu, J. Am. Chem. Soc. 136 (2014) 8438–8449.
- [2] S.K. Dutta, S.K. Mehetor, N. Pradhan, J. Phys. Chem. Lett. 6 (2015) 936–944.
- [3] L. Amirav, A.P. Alivisatos, J. Am. Chem. Soc. 135 (2013) 13049–13053.
- [4] W.R. Erwin, H.F. Zarick, E.M. Talbert, R. Bardhan, Energy Environ. Sci. 9 (2016) 1577–1601.
- [5] K. Zhu, N. Kopidakis, N.R. Neale, J. van de Lagemaat, A.J. Frank, J. Phys. Chem. B 110 (2006) 25174–25180.
- [6] X. Xu, C. Tang, H. Zeng, T. Zhai, S. Zhang, H. Zhao, Y. Bando, D. Golberg, A.C.S. Appl. Mater. Interfaces 3 (2011) 1352–1358.
- [7] H. Zeng, W. Cai, P. Liu, X. Xu, H. Zhou, C. Klingshirn, H. Kalt, ACS Nano 2 (2008) 1661–1670.
- [8] S. Ghosh, S. Khamarui, M. Saha, S.K. De, RSC Adv. 5 (2015) 38971–38976.
- [9] T. Wu, G. Liu, H. Hidaka, N. Serpone, J. Zhao, J. Phys. Chem. B. 102 (1998) 5845–5851.
- [10] J. Wang, Z. Lin, Chem. Mater. 22 (2010) 579–584.
- [11] A. Kar, S. Sain, D. Rossouw, B.R. Knappett, S.K. Pradhan, A.E.H. Wheatley, Nanoscale 8 (2016) 2727–2739.
- [12] Y. Xie, G. Ali, S.H. Yoo, S.O. Cho, A.C.S. Appl. Mater. Interfaces 2 (2010) 2910–2914.

- [13] K. Ma, O. Yehezkel, D.W. Domaille, H.H. Funke, J.N. Cha, *Angew. Chem. Int. Ed.* 54 (2015) 11490–11494.
- [14] C. Ratanatawanate, Y. Tao, K.J. Balkus, Jr., *J. Phys Chem. C* 113 (2009) 10755–10760.
- [15] W. Ma, L. Wang, N. Zhang, D. Han, Xiandui Dong, L. Niu, *Anal. Chem.* 87 (2015) 4844–4850.
- [16] S. Bai, L. Wang, X. Chen, J. Du, Yujie Xiong, *Nano Res.* 8 (2015) 175–183.
- [17] G. Lee, M. Kang, *Curr. Appl. Phys.* 13 (2013) 1482–1489.
- [18] J. Fang, L. Xu, Z. Zhang, Y. Yuan, S. Cao, Z. Wang, L. Yin, Y. Liao, C. Xue, *A.C.S. Appl. Mater. Interfaces* 5 (2013) 8088–8092.
- [19] V. Calzia, R. Piras, A. Ardu, A. Musinu, M. Saba, G. Bongiovanni, A. Mattoni, *J. Phys. Chem. C* 119 (2015) 16913–16919.
- [20] P. Lv, W. Fu, H. Yang, Y. H. Sun, J. Chen, X. Ma, L. Zhou, W. Tian, M. Zhang, H. Yao Li, D. Wu, *CrystEngComm* 15 (2013) 7548–7555.
- [21] G. Ai, R. Mo, Q. Chen, H. Xu, S. Yang, H. Li, J. Zhong, *RSC Adv.* 5 (2015) 13544–13549.
- [22] M. Lu, G. Yuan, Z. Wang, Y. Wang, J. Guo, *Appl. Catal. B: Environ.* 156–157 (2014) 25–34.
- [23] P. Han, A. Mihi, J. Ferre-borrull, J. Pallaréis, L.F. Marsal, *J. Phys. Chem. C* 119 (2015) 10693–10699.
- [24] T. Wu, X. Zhou, H. Zhangand, X. Zhong, *Nano Res.* 3 (2010) 379–386.
- [25] Suman Paul, Sirshendu Ghosh, Manas Saha, S.K. De, *Phys. Chem. Chem. Phys.* 18 (2016) 13092–13107.
- [26] S. Ghosh, M. Saha, S. Paul, S.K. De, *Nanoscale* 7 (2015) 18284–18298.
- [27] X. Zhang, Y. Lim Chen, R. Liu, D.P. Tsai, *Rep. Prog. Phys.* 76 (2013) 046401–046442.
- [28] G. Manna, R. Bose, N. Pradhan, *Angew. Chem. Int. Ed.* 53 (2014) 6743–6746.
- [29] Z.B. Yu, Y.P. Xie, G. Liu, G.Q. Liu (Max), X.L. Ma, H. Chenga, *J. Mater. Chem. A* 1 (2013) 2773–2776.
- [30] T.R. Gordon, R.E. Schaak, *Chem. Mater.* 26 (2014) 5900–5904.
- [31] J. Mohanta, S. Satapathy, S. Si, *ChemPhysChem* 17 (2016) 364–368.
- [32] C. Li, W. Fan, H. Lu, Y. Ge, H. Bai, W. Shi, *New J. Chem.* 40 (2016) 2287–2295.
- [33] Y. Zhao, K.T.E. Chua, C.K. Gan, J. Zhang, B. Peng, Z. Peng, Q. Xiong, *Phys. Rev. B* 84 (2011) 205330–205338.
- [34] B. Chen, C. Uher, L. Iordanidis, M.G. Kanatzidis, *Chem. Mater.* 9 (1997) 1655–1658.
- [35] D.J. Arenas, L.V. Gasparov, W. Qiu, J.C. Nino, C.H. Patterson, D.B. Tanner, *Phys. Rev. B* 82 (2010) 214302–214310.
- [36] D. Sarkar, S. Ishchuk, D.H. Taffa, N. Kaynan, B.A. Berke, T. Bendikov, R. Yerushalmi, *J. Phys. Chem. C* 120 (2016) 3853–3862.
- [37] A. Janotti, J.B. Varley, P. Rinke, N. Umezawa, G. Kresse, C.G. Van de Walle, *Phys. Rev. B* 81 (2010) 085212–085219.
- [38] J.C. Parker, R.W. Siegel, *Appl. Phys. Lett.* 57 (1990) 943–945.
- [39] X. Zhang, J. Qin, Yanan Xue, P. Yu, B. Zhang, L. Wang, R. Liu, *Sci. Rep.* 4 (2014) 4596–4604.
- [40] J. Liu, H. Yu, Z. Wu, W. Wang, J. Peng, Y. Cao, *Nanotechnology* 19 (2008) 345602–345611.
- [41] Z. Zhang, X. Zhong, S. Liu, D. Li, M. Han, *Angew. Chem.* 117 (2005) 3532–3536.
- [42] A. Narayanaswamy, H. Xu, N. Pradhan, X. Peng, *Angew. Chem.* 118 (2006) 5487–5490.
- [43] D.J. Riley, J.P. Waggett, K.G.U. Wijayantha, J. Mate, *Chem.* 14 (2004) 704–708.
- [44] D.O. Scanlon, C.W. Dunnill, J. Buckeridge, S.A. Shevlin, A.J. Logsdail, S. M.Woodley, C.R.A. Catlow, M.I. J. Powell, R.G. Palgrave, I.P. Parkin, G.W. Watson, T.W. Keal, P. Sherwood, Walsh, A.A. Sokol, *Nat. Mater.* 12 (2013) 798–801.
- [45] B. Enright, D. Fitzmaurice, *J. Phys. Chem.* 100 (1996) 1027–1035.
- [46] D.V. Talapin, R. Koeppen, S. Gotzinger, A. Kornowski, J.M. Lupton, A.L. Rogach, O. Benson, J. Feldmann, H. Weller, *Nano Lett.* 3 (2003) 1677–1681.
- [47] G. Zaiats, D. Yanover, R. Vaxenburg, J. Tilchin, A. Sashchiuk, E. Lifshitz, *Materials* 7 (2014) 7243–7275.
- [48] E. Khon, A. Mereshchenko, A.N. Tarnovsky, K. Acharya, A. Klinkova, N.N. Hewa-Kasakarage, I. Nemitz, M. Zamkov, *Nano Lett.* 11 (2011) 1792–1799.
- [49] H.T. Shabany, M.M. Nassary, M.S. El-Sadek, *J. Mater. Sci. Technol.* 24 (2008) 757–760.
- [50] Y. Wei, J. Jiao, Z. Zhao, W. Zhong, J. Li, J. Liu, G. Jiang, A. Duan, *J. Mater. Chem. A* 3 (2015) 11074–11085.
- [51] S.G. Babu, R. Vinoth, D.P. Kumar, M.V. Shankar, H. Chou, K. Vinodgopal, B. Neppolian, *Nanoscale* 7 (2015) 7849–7857.
- [52] Y. Shi, Y. Chen, G. Tian, H. Fu, K. Pan, J. Zhoua, H. Yana, *Dalton Trans.* 43 (2014) 12396–12404.
- [53] H. Kobayashi, T. Ueda, K. Miyakubo, T. Eguchiab, A. Tanib, *Phys. Chem. Chem. Phys.* 10 (2008) 1263–1269.
- [54] W. He, H. Kim, W.G. Wamer, D. Melka, J.H. Callahan, J. Yin, *J. Am. Chem. Soc.* 136 (2014) 750–757.
- [55] H. Jia, W. He, W.G. Wamer, X. Han, B. Zhang, S. Zhang, Z. Zheng, Y. Xiang, J. Yin, *J. Phys. Chem. C* 118 (2014) 21447–21456.
- [56] Y. Kano, K. Kushimoto, K. Komaguchi, Y. Ooyama, I. Imae, J. Ohshita, Y. Harima, *Phys. Chem. Chem. Phys.* 14 (2012) 15988–15990.
- [57] M. Wang, M. Ye, J. Iocozzia, C. Lin, Z. Lin, *Adv. Sci.* 3 (2016) 1600024–1600038.
- [58] R. Jiang, B. Li, C. Fang, J. Wang, *Adv. Mater.* 26 (2014) 5274–5309.
- [59] X. Ma, Y. Dai, L. Yu, B. Huang, *Light Sci. Appl.* (2016) 5.